Available online at www.sciencedirect.com
SCIENCE DIRECT®
Journal of Computational Physics 208 (2005) 570–615
JOURNAL OF COMPUTATIONAL PHYSICS
www.elsevier.com/locate/jcp

Accurate, efficient and monotonic numerical methods for multi-dimensional compressible flows Part II: Multi-dimensional limiting process

Kyu Hong Kim, Chongam Kim *

School of Mechanical and Aerospace Engineering, Seoul National University, Seoul 151-742, Republic of Korea

Received 16 February 2004; received in revised form 1 February 2005; accepted 28 February 2005
Available online 3 May 2005

Abstract

Through the analysis of conventional TVD limiters, a new multi-dimensional limiting function is derived for an oscillation control in multi-dimensional flows. And, multi-dimensional limiting process (MLP) is developed with the multi-dimensional limiting function. The major advantage of MLP is to prevent oscillations across a multi-dimensional discontinuity, and it is readily compatible with more than third order spatial interpolation. Moreover, compared with other higher order interpolation schemes such as ENO type schemes, MLP shows a good convergence characteristic in a steady problem and it is very simple to be implemented. In the present paper, third and fifth order interpolation schemes with MLP, named MLP3 and MLP5, are developed and tested for several real applications.

Through extensive numerous test cases including an oblique stationary contact discontinuity, an expansion fan, a vortex flow, a shock wave/vortex interaction and a viscous shock tube problem, it is verified that MLP combined with M-AUSMPW+ numerical flux substantially improves accuracy, efficiency and robustness both in continuous and discontinuous flows. By extending the current approach to three-dimensional flows, MLP is expected to reduce computational cost and enhance accuracy even further.

MSC: 35L65; 65M12; 76K05; 80A32

Keywords: Multi-dimensional limiting function; Multi-dimensional limiting process; Multi-dimensional flows; Entropy condition; Higher order spatial accuracy

* Corresponding author. Tel.: +82 2 880 1915; fax: +82 2 887 2662.
E-mail address: chongam@snu.ac.kr (C. Kim).

0021-9991/$ - see front matter © 2005 Elsevier Inc. All rights reserved.
doi:10.1016/j.jcp.2005.02.022

1. Introduction

At present stage, one of challenges in CFD is to provide an accurate and efficient solution in the analysis or design of three-dimensional aerodynamics. In order to cope with the requirement, a numerical scheme should be able to describe multi-dimensional flow phenomena as much as possible. However, up to now, most successful numerical methods, including spatial discretization and interpolation schemes, have been developed based on one-dimensional flow physics. Although this approach allows the rigorous analysis of numerical schemes, straightforward extension to two- or three-dimensional flows by dimensional splitting eventually leads to insufficient or excessive numerical dissipation, which in turn badly influences on the accuracy, robustness and convergence of numerical solutions. In other words, physically unacceptable interruption in numerics always results in the inaccurate representation of real physics.

In order to incorporate multi-dimensional physical phenomena, numerous approaches have been tried and developed by considering flow information along additional directions. Most notably, by modeling wave-speeds [1], rotating fluxes at a cell-interface [2–5], or by introducing fluctuation splitting and so on [6–8], various versions of multi-dimensional upwind fluxes have been developed. Obviously, a multi-dimensional scheme should bring noticeable improvement over conventional schemes in terms of accuracy. However, some degree of accuracy enhancement is compromised by robustness problem and computational cost, which is one of the obstacles in practical implementation. For example, most multi-dimensional schemes do not show monotonic behavior across a multi-dimensional discontinuity. When they are applied to high speed flow problems involving strong shocks, severe oscillations across strong shock are frequently generated and finally they may lead to a failure. One of the fundamental reasons, according to authors' experience, is that there is not an appropriate oscillation control method for a pure multi-dimensional problem. Thus, it is important to develop an oscillation control process based on multi-dimensional flow phenomena.

Concerning oscillation control schemes, so many studies have been carried out since the late 1970s and several important concepts, such as TVD, TVB, ENO, etc., have been proposed for better convergence and stable calculation. The concept of TVD (total variation diminishing) was proven to be extremely successful in solving hyperbolic conservation laws [9,10]. Although TVD criterion provides fundamental idea for oscillation control and is still very popular, conventional TVD schemes are somewhat unsatisfactory near extrema in terms of accuracy and convergence. In order to overcome this limitation, ENO (essentially non-oscillatory) schemes [11] and the concept of TVB (total variation bounded) [12] were introduced. The key idea of ENO schemes is to use the smoothest stencil among several candidates in evaluating fluxes at a cell boundary which should yield higher order spatial accuracy and essential non-oscillatory profile near shocks. TVB concept allows oscillations only if spurious oscillations do not grow unboundedly large as time evolves. Although TVB or ENO avoids unphysical clipping at extrema and enhances accuracy, it is inevitable to yield undershoot and/or overshoot which in turn influences convergence badly.

Most oscillation-free schemes have been based on the mathematical analysis of one-dimensional convection equation and applied to system of equations with the help of some linearization step. Also, they are applied to multi-dimensional applications with dimensional splitting. Although they may work successfully in many cases, it is insufficient or almost impossible to control oscillations near shock discontinuity in multi-space dimensions. For that reason, the need of oscillation control method for multi-dimensional applications is obvious.

The objective of the present paper is to develop a higher order limiting process which can control oscillations in multi-dimensional situations and be applicable to both unsteady and steady problems. In this respect, convergence is an important factor. Firstly, we derive a multi-dimensional limiting function to control oscillations. For that purpose, we adopt TVD concept as a starting point since it shows a better convergence characteristic among available oscillation control methods. And, a higher order polynomial interpolation combined with the multi-dimensional limiting function, called multi-dimensional limiting

process (MLP), is developed which possesses a higher degree of accuracy, computational efficiency and convergence.

The overall characteristics of MLP are summarized as follows:

- Oscillation control in multi-dimensional problems (multi-dimensional limiting process).
- Robust convergence characteristic with the help of multi-dimensional limiting function.
- Higher spatial accuracy (more than second order TVD scheme).
- Similar level of computational efficiency compared to conventional TVD MUSCL approach.

The direct comparison of MLP with other higher order interpolation schemes may be somewhat difficult because MLP equally emphasizes convergence, accuracy and efficiency in multi-dimensional flow situation. As a successful higher order interpolation scheme, several versions of ENO/WENO interpolation are developed [11,13–16] and widely used. The advantage of ENO/WENO is that more than third order spatial accuracy may be maintained even in local extrema. However, it shows oscillatory behavior and some convergence problems in a multi-dimensional shock discontinuity because it does not consider multi-dimensional flow situation. On the other hand, with the multi-dimensional limiting function, MLP can prevent oscillations in shock region and provide a good convergence characteristic. Simultaneously, MLP combined with M-AUSMPW+ may maintain higher order spatial accuracy like ENO/WENO in smooth region though the overall accuracy of MLP in discontinuity may be somewhat lower than ENO/WENO. In addition, it is very efficient to be implemented and yields very acceptable computational cost compared with conventional TVD MUSCL approaches because MLP adopts fixed and relatively compact stencil.

The present paper is organized as follows: After a brief description on the governing equations and basic spatial discretization in Section 2, the multi-dimensional limiting function is derived and MLP is described in detail in Section 3. In Section 4, numerous test cases are presented to verify the characteristics of MLP. Finally conclusions based on the numerical tests and analyses of the previous sections are drawn.

2. Governing equations and spatial discretization (M-AUSMPW+)

The two-dimensional Navier–Stokes equations in a conservative form is used as

$$\frac{\partial \mathbf{Q}}{\partial t}+\frac{\partial \mathbf{E}}{\partial x}+\frac{\partial \mathbf{F}}{\partial y}=\left(\frac{\partial \mathbf{E}_v}{\partial x}+\frac{\partial \mathbf{F}_v}{\partial y}\right), \tag{1}$$

where the flow and flux vectors are

$$\mathbf{Q}=\begin{pmatrix} \rho \\ \rho u \\ \rho v \\ \rho e_t \end{pmatrix}, \quad \mathbf{E}=\begin{pmatrix} \rho u \\ \rho u^2+p \\ \rho uv \\ (\rho e_t+p)u \end{pmatrix}, \quad \mathbf{F}=\begin{pmatrix} \rho v \\ \rho vu \\ \rho v^2+p \\ (\rho e_t+p)v \end{pmatrix}, \quad \mathbf{E}_v=\begin{pmatrix} 0 \\ \tau_{xx} \\ \tau_{xy} \\ e_v \end{pmatrix}, \quad \mathbf{F}_v=\begin{pmatrix} 0 \\ \tau_{xy} \\ \tau_{yy} \\ f_v \end{pmatrix} \tag{2}$$

with $e_v = u\,\tau_{xx} + v\,\tau_{xy} - q_x$, $f_v = u\,\tau_{xy} + v\,\tau_{yy} - q_y$. For calorically perfect gas, the equation of state is given by

$$p=(\gamma-1)\,\rho e=(\gamma-1)\,\rho\left(e_t-\frac{1}{2}\left(u^2+v^2\right)\right) \tag{3}$$

with $\gamma = 1.4$ for air.

As a baseline scheme, M-AUSMPW+ developed in Part I is adopted as follows:

$$\mathbf{F}_{\frac{1}{2}}=\bar{M}_{\mathrm{L}}^{+}c_{\frac{1}{2}}\boldsymbol{\Psi}_{\mathrm{L},\frac{1}{2}}+\bar{M}_{\mathrm{R}}^{-}c_{\frac{1}{2}}\boldsymbol{\Psi}_{\mathrm{R},\frac{1}{2}}+\left(P_{\mathrm{L}}^{+}\mathbf{P}_{\mathrm{L}}+P_{\mathrm{R}}^{-}\mathbf{P}_{\mathrm{R}}\right), \tag{4a}$$

where $\mathbf{P}_{L,R} = (0, n_x p_{L,R}, n_y p_{L,R}, 0)^T$ and $n_{x,y}$ are the components of the normal vector at a cell-interface. The vector of $\boldsymbol{\Psi}_{L,R,\frac{1}{2}}$ is the transferred property at a cell-interface which is given as follows:

$$\boldsymbol{\Psi}_{L,R,\frac{1}{2}} = \begin{pmatrix} \rho_{L,R,\frac{1}{2}} \\ \rho_{L,R,\frac{1}{2}} u_{L,R,\frac{1}{2}} \\ \rho_{L,R,\frac{1}{2}} v_{L,R,\frac{1}{2}} \\ \rho_{L,R,\frac{1}{2}} H_{L,R,\frac{1}{2}} \end{pmatrix}, \tag{4b}$$

where $H_{L,R,\frac{1}{2}} = \frac{\gamma}{\gamma-1}\frac{p_{L,R,\frac{1}{2}}}{\rho_{L,R,\frac{1}{2}}} + 0.5\left(u^2_{L,R,\frac{1}{2}} + v^2_{L,R,\frac{1}{2}}\right)$.

The detailed procedure including the Mach number interpolation function and pressure splitting function are explained in Part I [17]. The basic idea of the method is to re-evaluate the convective property, $\boldsymbol{\Psi}$, appropriately in smooth region to represent physical distribution more accurately. $\boldsymbol{\Psi}_{\frac{1}{2}}$ is reconstructed using the primitive variable vector at a cell interface, $\boldsymbol{\Phi}_{\frac{1}{2}} = (\rho_{\frac{1}{2}}, u_{\frac{1}{2}}, v_{\frac{1}{2}}, p_{\frac{1}{2}})^T$ which is summarized as follows:

$$\boldsymbol{\Phi}_{L,\frac{1}{2}} = \boldsymbol{\Phi}_L + \frac{\max\left[0, (\boldsymbol{\Phi}_R - \boldsymbol{\Phi}_L)\left(\boldsymbol{\Phi}_{L,\text{sup erbee}} - \boldsymbol{\Phi}_L\right)\right]}{(\boldsymbol{\Phi}_R - \boldsymbol{\Phi}_L)\left|\boldsymbol{\Phi}_{L,\text{sup erbee}} - \boldsymbol{\Phi}_L\right|} \min\left[a\frac{|\boldsymbol{\Phi}_R - \boldsymbol{\Phi}_L|}{2}, \left|\boldsymbol{\Phi}_{L,\text{sup erbee}} - \boldsymbol{\Phi}_L\right|\right], \tag{5a}$$

$$\boldsymbol{\Phi}_{R,\frac{1}{2}} = \boldsymbol{\Phi}_R + \frac{\max\left[0, (\boldsymbol{\Phi}_L - \boldsymbol{\Phi}_R)\left(\boldsymbol{\Phi}_{R,\text{sup erbee}} - \boldsymbol{\Phi}_R\right)\right]}{(\boldsymbol{\Phi}_L - \boldsymbol{\Phi}_R)\left|\boldsymbol{\Phi}_{R,\text{sup erbee}} - \boldsymbol{\Phi}_R\right|} \min\left[a\frac{|\boldsymbol{\Phi}_L - \boldsymbol{\Phi}_R|}{2}, \left|\boldsymbol{\Phi}_{R,\text{sup erbee}} - \boldsymbol{\Phi}_R\right|\right], \tag{5b}$$

where $a = 1 - \min(1, \max(|M_L|, |M_R|))^2$ and $\boldsymbol{\Phi}_L$ and $\boldsymbol{\Phi}_R$ are values calculated by an interpolation scheme. The detail is referred to Part I. Similar to Part I, all the vector notations in Part II are introduced for compact expression. Thus, in actual implementation, they should be applied component by component.

3. Multi-dimensional limiting process (MLP)

In developing MLP, monotonicity in multi-space dimensions, more than third order spatial interpolation and good convergence are the main factors to be taken into account. Firstly, through the analysis of conventional TVD limiters, the multi-dimensional limiting function is derived. And, secondly third and fifth order interpolation combined with the multi-dimensional limiting function is introduced in Section 3.3.

3.1. Examination of TVD MUSCL limiter

In view of Godunov-type approach, the steps to construct a numerical flux at a cell-interface usually consist of interpolation stage and evaluation stage. It is known that interpolation stage is generally independent of evaluation stage where the local Riemann problem is solved at a cell interface. Thus, for higher order spatial accuracy, interpolation stage is modified without changing a Riemann solver. Referring that piecewise constant state generates first order spatial accuracy, a piecewise linear or quadratic distribution is applied for second or third spatial accuracy. This method for the generation of second order upwind schemes is often referred as the MUSCL approach [18]. In view of FVS (flux vector splitting) and AUSM-type schemes, the evaluation stage corresponds to the flux splitting step.

MUSCL approach with TVD limiter is written as follows:

$$\boldsymbol{\Phi}_L = \bar{\boldsymbol{\Phi}}_i + \frac{1}{4}\left[(1-\,\,)\phi(r_L) + (1+\,\,)r_L\phi\left(\frac{1}{r_L}\right)\right]\left(\bar{\boldsymbol{\Phi}}_i - \bar{\boldsymbol{\Phi}}_{i-1}\right), \tag{6a}$$

$$\boldsymbol{\Phi}_{\mathrm{R}} = \bar{\boldsymbol{\Phi}}_{i+1} - \frac{1}{4}\left[(1-\,)\phi(r_{\mathrm{R}}) + (1+\,)r_{\mathrm{R}}\phi\left(\frac{1}{r_{\mathrm{R}}}\right)\right]\left(\bar{\boldsymbol{\Phi}}_{i+2} - \bar{\boldsymbol{\Phi}}_{i+1}\right), \tag{6b}$$

where $\boldsymbol{\Phi}$ is a property vector, $r_{\mathrm{L}} = \frac{\bar{\boldsymbol{\Phi}}_{i+1} - \bar{\boldsymbol{\Phi}}_i}{\bar{\boldsymbol{\Phi}}_i - \bar{\boldsymbol{\Phi}}_{i-1}}$ and $r_{\mathrm{R}} = \frac{\bar{\boldsymbol{\Phi}}_{i+1} - \bar{\boldsymbol{\Phi}}_i}{\bar{\boldsymbol{\Phi}}_{i+2} - \bar{\boldsymbol{\Phi}}_{i+1}}$.

The bar means cell averaged value and is a TVD limiter which monitors the local gradient of property and determines local slope under monotonic condition. The calculated value has third order spatial accuracy with = 1/3.

As known well, if TVD limiter is symmetric, Eq. (6) is independent of and simplified as follows:

$$\boldsymbol{\Phi}_{\mathrm{L}} = \bar{\boldsymbol{\Phi}}_i + 0.5\phi(r_{\mathrm{L}})\left(\bar{\boldsymbol{\Phi}}_i - \bar{\boldsymbol{\Phi}}_{i-1}\right), \tag{7a}$$

$$\boldsymbol{\Phi}_{\mathrm{R}} = \bar{\boldsymbol{\Phi}}_{i+1} - 0.5\phi(r_{\mathrm{R}})\left(\bar{\boldsymbol{\Phi}}_{i+2} - \bar{\boldsymbol{\Phi}}_{i+1}\right), \tag{7b}$$

where $\phi(r) = r\phi(1/r)$.

In flows including physical discontinuities, ϕ is definitely employed to yield monotonic distribution. Eqs. (8)–(10) show well-known existing TVD limiters.

Minmod limiter:

$$\phi(r) = \max(0, \min(r, 1)). \tag{8}$$

van Leer limiter:

$$\phi(r) = \frac{r + |r|}{1 + |r|}. \tag{9}$$

Superbee limiter:

$$\phi(r) = \max(0, \min(2r, 1), \min(r, 2)). \tag{10}$$

Here, we examine some characteristics of typical TVD limiters closely and discuss the influence of flow physics on interpolation stage. It is assumed that a property distribution increases monotonically with ($\partial\boldsymbol{\Phi}/\partial x > 0$ and $\partial^2\boldsymbol{\Phi}/\partial x^2 > 0$) as in Fig. 1. Other situations such as ($\partial\boldsymbol{\Phi}/\partial x > 0$ and $\partial^2\boldsymbol{\Phi}/\partial x^2 < 0$), ($\partial\boldsymbol{\Phi}/\partial x < 0$ and $\partial^2\boldsymbol{\Phi}/\partial x^2 > 0$) or ($\partial\boldsymbol{\Phi}/\partial x < 0$ and $\partial^2\boldsymbol{\Phi}/\partial x^2 < 0$) can be treated in a symmetric manner. Defining the variation at a cell-interface as $\Delta\boldsymbol{\Phi}_{i+\frac{1}{2}} = \bar{\boldsymbol{\Phi}}_{i+1} - \bar{\boldsymbol{\Phi}}_i$, the variation at a cell is determined by

$$\boldsymbol{\Phi}_{\mathrm{L}} = \bar{\boldsymbol{\Phi}}_i + 0.5\Delta\boldsymbol{\Phi}|_i = \bar{\boldsymbol{\Phi}}_i + 0.5\phi(r_{\mathrm{L}})\Delta\boldsymbol{\Phi}_{i-\frac{1}{2}}, \quad \Delta\boldsymbol{\Phi}|_i = \phi(r_{\mathrm{L}})\Delta\boldsymbol{\Phi}_{i-\frac{1}{2}}, \tag{11a}$$

$$\boldsymbol{\Phi}_{\mathrm{R}} = \bar{\boldsymbol{\Phi}}_{i+1} - 0.5\Delta\boldsymbol{\Phi}|_{i+1} = \bar{\boldsymbol{\Phi}}_{i+1} - 0.5\phi(r_{\mathrm{R}})\Delta\boldsymbol{\Phi}_{i+\frac{3}{2}}, \quad \Delta\boldsymbol{\Phi}|_{i+1} = \phi(r_{\mathrm{R}})\Delta\boldsymbol{\Phi}_{i+\frac{3}{2}}, \tag{11b}$$

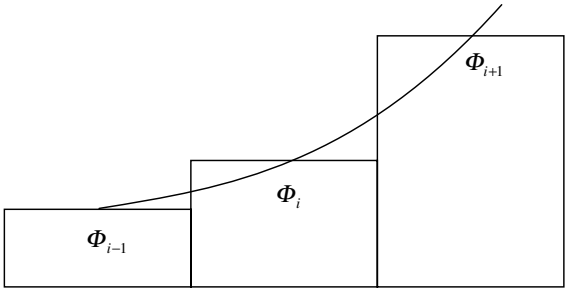

Fig. 1. Monotonically increasing property distribution.

where $r_{\mathrm{L}} = \frac{\Delta\boldsymbol{\Phi}_{i+\frac{1}{2}}}{\Delta\boldsymbol{\Phi}_{i-\frac{1}{2}}}$ and $r_{\mathrm{R}} = \frac{\Delta\boldsymbol{\Phi}_{i+\frac{1}{2}}}{\Delta\boldsymbol{\Phi}_{i+\frac{3}{2}}}$. From the distribution of $\partial\boldsymbol{\Phi}/\partial x > 0$ and $\partial^2\boldsymbol{\Phi}/\partial x^2 > 0$, the condition of $\Delta\boldsymbol{\Phi}_{i-\frac{1}{2}} < \Delta\boldsymbol{\Phi}_{i+\frac{1}{2}} < \Delta\boldsymbol{\Phi}_{i+\frac{3}{2}}$ is satisfied and the ratios of variation, r_{L} and r_{R}, have the following values:

$$r_{\mathrm{L}} = \frac{\Delta\boldsymbol{\Phi}_{i+\frac{1}{2}}}{\Delta\boldsymbol{\Phi}_{i-\frac{1}{2}}} > 1, \quad r_{\mathrm{R}} = \frac{\Delta\boldsymbol{\Phi}_{i+\frac{1}{2}}}{\Delta\boldsymbol{\Phi}_{i+\frac{3}{2}}} < 1 \quad \text{and} \quad r_{\mathrm{L}} < \frac{1}{r_{\mathrm{R}}}. \tag{12}$$

From the results of Part I, the interpolated values of minmod and superbee limiter satisfy the following conditions:

$$\bar{\boldsymbol{\Phi}}_i < \boldsymbol{\Phi}_{\mathrm{L,min\ mod}} < \boldsymbol{\Phi}_{\mathrm{real},i+\frac{1}{2}} < \boldsymbol{\Phi}_{\mathrm{R,min\ mod}} < \bar{\boldsymbol{\Phi}}_{i+1}, \tag{13a}$$

$$\bar{\boldsymbol{\Phi}}_i < \boldsymbol{\Phi}_{\mathrm{R,sup\ erbee}} < \boldsymbol{\Phi}_{\mathrm{real},i+\frac{1}{2}} < \boldsymbol{\Phi}_{\mathrm{L,sup\ erbee}} < \bar{\boldsymbol{\Phi}}_{i+1}, \quad (1 < r_{\mathrm{L}} < 2), \tag{13b}$$

$$\bar{\boldsymbol{\Phi}}_i = \boldsymbol{\Phi}_{\mathrm{R,sup\ erbee}} < \boldsymbol{\Phi}_{\mathrm{L,sup\ erbee}} < \bar{\boldsymbol{\Phi}}_{i+1}, \quad (r_{\mathrm{L}} > 2),$$

where the subscript 'real' indicates the exact physical value and the detailed is referred to Part I of the present papers.

And we have

Minmod limiter:

$$\Delta\boldsymbol{\Phi}|_i = \min\left(\Delta\boldsymbol{\Phi}_{i-\frac{1}{2}}, \Delta\boldsymbol{\Phi}_{i+\frac{1}{2}}\right) = \Delta\boldsymbol{\Phi}_{i-\frac{1}{2}}, \quad \Delta\boldsymbol{\Phi}|_{i+1} = \min\left(\Delta\boldsymbol{\Phi}_{i+\frac{1}{2}}, \Delta\boldsymbol{\Phi}_{i+\frac{3}{2}}\right) = \Delta\boldsymbol{\Phi}_{i+\frac{1}{2}}. \tag{14}$$

Superbee limiter:

$$\Delta\boldsymbol{\Phi}|_i = \min\left(2\Delta\boldsymbol{\Phi}_{i-\frac{1}{2}}, \Delta\boldsymbol{\Phi}_{i+\frac{1}{2}}\right), \quad \Delta\boldsymbol{\Phi}|_{i+1} = \min\left(2\Delta\boldsymbol{\Phi}_{i+\frac{1}{2}}, \Delta\boldsymbol{\Phi}_{i+\frac{3}{2}}\right). \tag{15a}$$

Especially in a rapidly varied region,

$$\Delta\boldsymbol{\Phi}|_i = 2\Delta\boldsymbol{\Phi}_{i-\frac{1}{2}}, \quad \Delta\boldsymbol{\Phi}|_{i+1} = 2\Delta\boldsymbol{\Phi}_{i+\frac{1}{2}}, \tag{15b}$$

where $r_{\mathrm{L}} > 2$ and $r_{\mathrm{R}} < \frac{1}{r_{\mathrm{L}}} < 0.5$.

In discontinuous region, $\partial\boldsymbol{\Phi}/\partial x$ needs to be calculated as large as possible since the slope of discontinuity is infinite mathematically. That is, $\Delta\boldsymbol{\Phi}|_i$ and $\Delta\boldsymbol{\Phi}|_{i+1}$ should be maximized. From this viewpoint, superbee limiter is advantageous. In shock discontinuity, because of compression effect, shock profiles calculated by MUSCL limiters are similar to each other. However, contact discontinuity in multi-space dimensions is smeared much because of numerical dissipation. (See Figs. 17 and 18 of Part I or Figs. 11 and 12 of Part II.) Thus, the resolution of contact discontinuities is very dependent on TVD limiters. Since $r_{\mathrm{L}} > 2$ and $r_{\mathrm{R}} < 0.5$ generally belong to the head and tail of a numerical discontinuity, the slope of superbee limiter is about twice steeper than minmod case as shown in Eqs. (14) and (15b). As a result, superbee limiter can provide about four times and eight times grid point reduction effect in two- and three-dimensional problems, which is shown in Figs. 17 and 18 of Part I.

On the other hand, in continuous region, we need optimal slope which can predict the real physical value accurately. As seen from Eq. (13), the range of optimal slope lies between $\Delta\boldsymbol{\Phi}_{\mathrm{minmod}}$ and $\Delta\boldsymbol{\Phi}_{\mathrm{superbee}}$. Thus, unlike from discontinuous region, it cannot be said that superbee limiter is more advantageous than minmod limiter in continuous region. More generally, it can be observed that steeper slope than the real physical slope yields the entropy increasing situation in isentropic compressible flow and the entropy decreasing situation in isentropic expansion flow. In contrast, gentler slope exhibits exactly opposite behavior. We show this observation in case of isentropic expansion flow. The other case can be shown similarly.

The speed of sound in isentropic condition is written as follows:

$$\left(\frac{\partial p}{\partial}\right)_s = c^2 = \gamma \frac{p}{} = \gamma RT, \tag{16}$$

where R is a gas constant.

For isentropic flow, the equation of state can be written as

$$p^{-\gamma} = \text{const.} \tag{17}$$

Then, the following relation can be obtained.

$$\frac{p_{\text{real},i+\frac{1}{2}}}{p_{\text{real},i}}\left(\frac{\text{real},i+\frac{1}{2}}{\text{real},i}\right)^{-\gamma} = 1, \quad \frac{p_{\text{real},i+\frac{1}{2}}}{\text{real},i+\frac{1}{2}} = \frac{p_{\text{real},i}}{\text{real},i}\left(\frac{\text{real},i+\frac{1}{2}}{\text{real},i}\right)^{\gamma-1}. \tag{18}$$

Since fluid should move isentropically from a cell center point i to a cell-interface $i+\frac{1}{2}$,

$$\left.\frac{\partial p}{\partial}\right|_{\text{real},i} = \gamma \frac{p_{\text{real},i}}{\text{real},i} = \gamma RT_{\text{real},i}. \tag{19}$$

$$\left.\frac{\partial p}{\partial}\right|_{\text{real},i+\frac{1}{2}} = \gamma RT_{\text{real},i+\frac{1}{2}} = \gamma RT_{\text{real},i}\left(\frac{\text{real},i+\frac{1}{2}}{\text{real},i}\right)^{\gamma-1}. \tag{20}$$

In expansion flow, $\partial\ /\partial x$ and $\partial T/\partial x$ are negative, and from Eq. (13), density and temperature distributions are as follows:

$$_{\text{real},i} > \ _{i+\frac{1}{2},\text{min mod}} > \ _{\text{real},i+\frac{1}{2}} > \ _{i+\frac{1}{2},\text{sup erbee}} > \ _{\text{real},i+1}, \tag{21}$$

$$T_{\text{real},i} > T_{i+\frac{1}{2},\text{min mod}} > T_{\text{real},i+\frac{1}{2}} > T_{i+\frac{1}{2},\text{sup erbee}} > T_{\text{real},i+1}. \tag{22}$$

Since all processes from the cell center point i to $i+1$ should be isentropic and $T_{i+\frac{1}{2},\text{min mod}}$ is greater than $T_{\text{real},i+\frac{1}{2}}$, minmod limiter always increases entropy in isentropic expansion flow as

$$\left.\frac{\partial p}{\partial}\right|_{i+\frac{1}{2},\text{min mod}} = \gamma RT_{i+\frac{1}{2},\text{min mod}} > \gamma RT_{\text{real},i+\frac{1}{2}} = \left.\frac{\partial p}{\partial}\right|_{\text{real},i+\frac{1}{2}}, \tag{23}$$

or

$$\left.\frac{\partial p}{\partial}\right|_{i+\frac{1}{2},\text{min mod}} = \gamma RT_{\text{real},i}\left(\frac{i+\frac{1}{2},\text{min mod}}{\text{real},i}\right)^{\gamma-1} > \gamma RT_{\text{real},i}\left(\frac{\text{real},i+\frac{1}{2}}{\text{real},i}\right)^{\gamma-1} = \left.\frac{\partial p}{\partial}\right|_{\text{real},i+\frac{1}{2}}, \tag{24}$$

where $\gamma = 1.4$.

And similarly, superbee limiter always decreases entropy as

$$\left.\frac{\partial p}{\partial}\right|_{i+\frac{1}{2},\text{sup erbee}} = \gamma RT_{i+\frac{1}{2},\text{sup erbee}} < \gamma RT_{\text{real},i+\frac{1}{2}} = \left.\frac{\partial p}{\partial}\right|_{\text{real},i+\frac{1}{2}}, \tag{25}$$

or

$$\left.\frac{\partial p}{\partial}\right|_{i+\frac{1}{2},\text{sup erbee}} = \gamma RT_{\text{real},i}\left(\frac{i+\frac{1}{2},\text{sup erbee}}{\text{real},i}\right)^{\gamma-1} < \gamma RT_{\text{real},i}\left(\frac{\text{real},i+\frac{1}{2}}{\text{real},i}\right)^{\gamma-1} = \left.\frac{\partial p}{\partial}\right|_{\text{real},i+\frac{1}{2}}. \tag{26}$$

Generally, even though entropy in evolution stage is always produced by numerical fluxes such as Roe-type with entropy fix or AUSM-type schemes, the net change of entropy after iteration can be negative due to the entropy decreasing mechanism at interpolation step. The test cases of expansion fan or vortex flow using superbee limiter (Sections 4.3 and 4.4) would be a typical example.

Minmod limiter also decreases entropy in isentropic compression flow. However, we are more concerned with expansion flow case since negative entropy variation in isentropic expansion flow can be sustained without lower bound as computation continues. This can be seen in the test case of vortex flow. Physically, entropy variation should be bounded between zero and the maximum positive value. The maximum positive value is determined by the governing conservation laws and the corresponding conservative discretization, but the minimum value of zero is imposed by the second thermodynamic law which is not considered explicitly in computations. Thus, in actual computations, entropy can be decreased without lower bound which leads to the failure of calculations. On the other hand, entropy cannot grow continuously without upper bound because the conservative discretized form of the governing equations precludes it by the action of a shock wave.

Interpolation step is generally considered to be independent of flow physics and only related to mathematics. Thus, up to now, the entropy condition has been considered only at evaluation stage. However, if we use the same limiter both in isentropic compression and isentropic expansion flows, one of cases definitely brings negative entropy variation at interpolation step. In many applications, negative entropy variation is not amplified and makes no serious problem. However, it can not be guaranteed in cases involving strong expansion. Therefore, flow physics such as the entropy condition is critical both at evolution stage and at interpolation stage. In the present paper, it is certified through the analysis of this section and lots of numerical experiments in Section 4.

3.2. Higher order TVD interpolation

Judging from the result of the previous section, optimal slope should be able to preclude entropy decreasing solution. The reason for the excessive variation of superbee limiter in continuous region is that the slope is chosen without any consideration of curvature distribution. When second order MUSCL approach is applied, there is no concrete information on the variation of $\Delta\boldsymbol{\Phi}_{\text{optimal}}|_i$, except for the monotonic constraint of $\min(\Delta\boldsymbol{\Phi}_{i-\frac{1}{2}}, \Delta\boldsymbol{\Phi}_{i+\frac{1}{2}}) < \Delta\boldsymbol{\Phi}_{\text{optimal}}|_i < \max(\Delta\boldsymbol{\Phi}_{i-\frac{1}{2}}, \Delta\boldsymbol{\Phi}_{i+\frac{1}{2}})$. It is intrinsically problematic in the second order interpolation schemes. For example, superbee limiter always chooses the lager variation of two candidates and minmod limiter always chooses the smaller one without considering real physical situation.

Let optimal variation be

$$\Delta\boldsymbol{\Phi}_{\text{optimal}}\big|_i = \beta\Delta\boldsymbol{\Phi}_{i-\frac{1}{2}}, \tag{27}$$

where β has to be specified. Improper choice of β would yield dissipative or entropy-violating result as in case of minmod or superbee limiter. In order to determine β based on flow physics, more than third order spatial interpolation is essential because the second order interpolation cannot reflect the curvature of $\boldsymbol{\Phi}$.

3.2.1. Third order interpolation with TVD limiting

Similar to reconstruction by the primitive function in ENO [11], third order interpolation which satisfies the conservation requirement is applied. For equally spacing grid points, $\boldsymbol{\Phi}$ is given by

$$\boldsymbol{\Phi}(x) = ax^2 + bx + c. \tag{28}$$

And, the cell-averaged value is (see Fig. 2)

$$\frac{1}{\Delta x}\int_{(m-1)\Delta x}^{m\Delta x} \boldsymbol{\Phi}(x)\mathrm{d}x = \bar{\boldsymbol{\Phi}}_{i+m} \quad (m = -1, 0, 1). \tag{29}$$

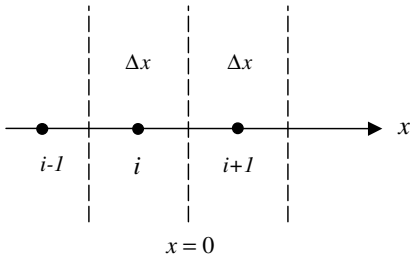

Fig. 2. Cell center point and cell-interface.

Then, from Eqs. (28) and (29), the value of $\boldsymbol{\Phi}$ at a cell-interface is written as follows:

$$\boldsymbol{\Phi}_{i+\frac{1}{2}} = \frac{2\bar{\boldsymbol{\Phi}}_{i+1} + 5\bar{\boldsymbol{\Phi}}_i - \bar{\boldsymbol{\Phi}}_{i-1}}{6} = \bar{\boldsymbol{\Phi}}_i + 0.5\frac{\Delta\boldsymbol{\Phi}_{i-\frac{1}{2}} + 2\Delta\boldsymbol{\Phi}_{i+\frac{1}{2}}}{3} = \bar{\boldsymbol{\Phi}}_i + 0.5\beta(r_i)\Delta\boldsymbol{\Phi}_{i-\frac{1}{2}}, \tag{30}$$

where $\beta = \frac{1+2r_i}{3}$ and $r_i = \frac{\Delta\boldsymbol{\Phi}_{i+\frac{1}{2}}}{\Delta\boldsymbol{\Phi}_{i-\frac{1}{2}}}$.

To suppress oscillations across a discontinuity, TVD limiting condition of $\max(0, \min(2,2r))$ is applied to Eq. (30) [10]. Then, the higher order interpolation filtered by TVD limiting can be written as

$$\phi(r) = \max(0, \min(2, 2r, \beta)). \tag{31}$$

Finally, left and right cell-interface values are obtained as follows:

$$\boldsymbol{\Phi}_{\mathrm{L}} = \bar{\boldsymbol{\Phi}}_i + 0.5\phi(r_{\mathrm{L},i})\Delta\boldsymbol{\Phi}_{i-\frac{1}{2}} = \bar{\boldsymbol{\Phi}}_i + 0.5\max(0, \min(2, 2r_{\mathrm{L},i}, \beta_{\mathrm{L}}))\Delta\boldsymbol{\Phi}_{i-\frac{1}{2}}, \tag{32a}$$

$$\boldsymbol{\Phi}_{\mathrm{R}} = \bar{\boldsymbol{\Phi}}_{i+1} - 0.5\phi(r_{\mathrm{R},i+1})\Delta\boldsymbol{\Phi}_{i+\frac{3}{2}} = \bar{\boldsymbol{\Phi}}_{i+1} - 0.5\max(0, \min(2, 2r_{\mathrm{R},i+1}, \beta_{\mathrm{R}}))\Delta\boldsymbol{\Phi}_{i+\frac{3}{2}}. \tag{32b}$$

In Eq. (32), β_{L} and β_{R} are given as follows:

$$\beta_{\mathrm{L}} = \frac{1+2r_{\mathrm{L},i}}{3}, \quad \beta_{\mathrm{R}} = \frac{1+2r_{\mathrm{R},i+1}}{3}, \tag{33}$$

where $r_{\mathrm{L},i} = \frac{\Delta\boldsymbol{\Phi}_{i+\frac{1}{2}}}{\Delta\boldsymbol{\Phi}_{i-\frac{1}{2}}}$ and $r_{\mathrm{R},i+1} = \frac{\Delta\boldsymbol{\Phi}_{i+\frac{1}{2}}}{\Delta\boldsymbol{\Phi}_{i+\frac{3}{2}}}$.

3.2.2. Fifth order interpolation with TVD limiting

In a similar way, fifth order interpolation can be obtained as

$$\boldsymbol{\Phi}(x) = ax^4 + bx^3 + cx^2 + dx + e. \tag{34}$$

And, the interpolated value $\boldsymbol{\Phi}$ at a cell-interface is given by

$$\begin{aligned}\boldsymbol{\Phi}_{i+\frac{1}{2}} &= \frac{2\bar{\boldsymbol{\Phi}}_{i-2} - 13\bar{\boldsymbol{\Phi}}_{i-1} + 47\bar{\boldsymbol{\Phi}}_i + 27\bar{\boldsymbol{\Phi}}_{i+1} - 3\bar{\boldsymbol{\Phi}}_{i+2}}{60} \\ &= \bar{\boldsymbol{\Phi}}_i + 0.5\frac{-2\Delta\boldsymbol{\Phi}_{i-\frac{3}{2}} + 11\Delta\boldsymbol{\Phi}_{i-\frac{1}{2}} + 24\Delta\boldsymbol{\Phi}_{i+\frac{1}{2}} - 3\Delta\boldsymbol{\Phi}_{i+\frac{3}{2}}}{30} = \bar{\boldsymbol{\Phi}}_i + 0.5\beta(r_{i-1}, r_i, r_{i+1})\Delta\boldsymbol{\Phi}_{i-\frac{1}{2}},\end{aligned} \tag{35}$$

where $\beta = \frac{-2/r_{i-1}+11+24r_i-3r_ir_{i+1}}{30}$, $r_{i-1} = \frac{\Delta\boldsymbol{\Phi}_{i-\frac{1}{2}}}{\Delta\boldsymbol{\Phi}_{i-\frac{3}{2}}}$, $r_i = \frac{\Delta\boldsymbol{\Phi}_{i+\frac{1}{2}}}{\Delta\boldsymbol{\Phi}_{i-\frac{1}{2}}}$ and $r_{i+1} = \frac{\Delta\boldsymbol{\Phi}_{i+\frac{3}{2}}}{\Delta\boldsymbol{\Phi}_{i+\frac{1}{2}}}$. It is noted that β of fifth order interpolation is the function of r_{i-1}, r_i and r_{i+1}.

Finally, the fifth order interpolation scheme filtered by TVD limiting can be written as follows:

$$\boldsymbol{\Phi}_{\mathrm{L}} = \bar{\boldsymbol{\Phi}}_i + 0.5\phi(r_{\mathrm{L}})\Delta\boldsymbol{\Phi}_{i-\frac{1}{2}} = \bar{\boldsymbol{\Phi}}_i + 0.5\max(0, \min(2, 2r_{\mathrm{L},i}, \beta_{\mathrm{L}}))\Delta\boldsymbol{\Phi}_{i-\frac{1}{2}}, \tag{36a}$$

$$\boldsymbol{\Phi}_{\mathrm{R}} = \bar{\boldsymbol{\Phi}}_{i+1} - 0.5\phi(r_{\mathrm{R}})\Delta\boldsymbol{\Phi}_{i+\frac{3}{2}} = \bar{\boldsymbol{\Phi}}_{i+1} - 0.5\max(0, \min(2, 2r_{\mathrm{R},i+1}, \beta_{\mathrm{R}}))\Delta\boldsymbol{\Phi}_{i+\frac{3}{2}}. \tag{36b}$$

In Eq. (36), β_{L} and β_{R} is given as follows:

$$\beta_{\mathrm{L}} = \frac{-2/r_{\mathrm{L},i-1} + 11 + 24r_{\mathrm{L},i} - 3r_{\mathrm{L},i}r_{\mathrm{L},i+1}}{30}, \quad \beta_{\mathrm{R}} = \frac{-2/r_{\mathrm{R},i+2} + 11 + 24r_{\mathrm{R},i+1} - 3r_{\mathrm{R},i+1}r_{\mathrm{R},i}}{30}, \tag{37}$$

where $r_{\mathrm{L},i-1} = \frac{\Delta\boldsymbol{\Phi}_{i-\frac{1}{2}}}{\Delta\boldsymbol{\Phi}_{i-\frac{3}{2}}}$, $r_{\mathrm{L},i} = \frac{\Delta\boldsymbol{\Phi}_{i+\frac{1}{2}}}{\Delta\boldsymbol{\Phi}_{i-\frac{1}{2}}}$, $r_{\mathrm{L},i+1} = \frac{\Delta\boldsymbol{\Phi}_{i+\frac{3}{2}}}{\Delta\boldsymbol{\Phi}_{i+\frac{1}{2}}}$ and $r_{\mathrm{R},i+2} = \frac{\Delta\boldsymbol{\Phi}_{i+\frac{3}{2}}}{\Delta\boldsymbol{\Phi}_{i+\frac{5}{2}}}$, $r_{\mathrm{R},i+1} = \frac{\Delta\boldsymbol{\Phi}_{i+\frac{1}{2}}}{\Delta\boldsymbol{\Phi}_{i+\frac{3}{2}}}$, $r_{\mathrm{R},i} = \frac{\Delta\boldsymbol{\Phi}_{i-\frac{1}{2}}}{\Delta\boldsymbol{\Phi}_{i+\frac{1}{2}}}$.

3.3. Development of multi-dimensional limiting process (MLP)

Since the late 1970s, numerous ways to control oscillations have been studied and several limiting concepts have been proposed. Most representatives would be TVD, TVB and ENO. In case of scalar convection equation, rigorous mathematical analysis unveils their good characteristics. However, it looks very difficult to prove similar behaviors in non-linear systems of equations. Thus, the successful application of these approaches to multi-dimensional systems is largely based on some linearization step and some practical experience. Even though they can be applied successfully in many cases, some weakness is still observed in calculating shock discontinuity in multi-dimensional flow. Therefore, it is believed that the previous limiting concept based on one-dimensional flow physics has to be improved and a new limiting process has to be introduced based on multi-dimensional flow physics.

One of the fundamental difficulties in handling multi-dimensional problems is that it is difficult to define monotonic characteristic [19] and especially, the definition of monotonic distribution is ambiguous near a saddle point. In addition, Goodman and LeVeque [20] showed TVD scheme in two space dimensions can not be more than first order accurate. Thus, it looks nearly impossible to develop an oscillation control scheme with global higher order accuracy in multi-space dimensions. However, if we focus on more specific issue, the limitation of the previous oscillation control concept can be improved. For that reason, Spekreijse defined his own version of multi-dimensional monotonic condition, and derived a second order monotone upwind scheme which satisfies his multi-dimensional monotonic condition in steady case. The monotone scheme was analyzed based on a non-linear scalar equation [21]. Although it shows good performances in scalar convection equation, it does not seem to be good enough to control oscillations in multi-dimensional shock discontinuity and requires some unknown parameter.

In the present paper, we mainly focus on oscillation control across a multi-dimensional shock discontinuity to sidestep the difficulty in defining multi-dimensional monotonic distribution exactly. Then, a multi-dimensional limiting function is derived using nine point stencil as in Fig. 3. It is based on oscillation control concept because this is more flexible to deal with multi-dimensional situation than strict monotonic concept. TVD is adopted for that purpose.

3.3.1. Derivation of a multi-dimensional limiting function

One-dimensional limiting condition using TVD constraint can be written as follows [10].

$$0 \leqslant \phi(r) \leqslant \min(2r, 2). \tag{38}$$

Since the extension of Eq. (38) in a dimensional splitting manner is insufficient to prevent oscillations in multi-dimensional flow, it needs to be modified and/or extended with appropriate consideration of multi-dimensional situation. From Eqs. (38) and (7), the property at a cell-interface satisfies the following distribution.

$$\bar{\boldsymbol{\Phi}}_{i-1} \leqslant \boldsymbol{\Phi}_{i-\frac{1}{2}} \leqslant \bar{\boldsymbol{\Phi}}_{i}, \quad \bar{\boldsymbol{\Phi}}_{i} \leqslant \boldsymbol{\Phi}_{i+\frac{1}{2}} \leqslant \bar{\boldsymbol{\Phi}}_{i+1}. \tag{39a}$$

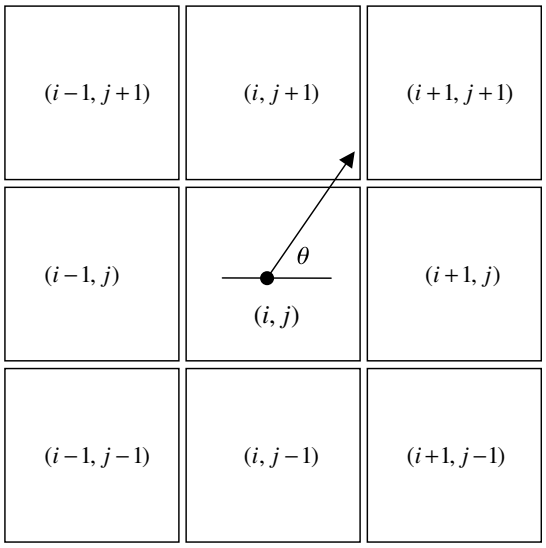

Fig. 3. Neighboring cells to derive the multi-dimensional limiting function.

Thus, the dimensional splitting extension of Eq. (39a) is

$$\bar{\Phi}_{i-1,j} \leqslant \Phi_{i-\frac{1}{2},j} \leqslant \bar{\Phi}_{i,j}, \quad \bar{\Phi}_{i,j} \leqslant \Phi_{i+\frac{1}{2},j} \leqslant \bar{\Phi}_{i+1,j}, \quad \bar{\Phi}_{i,j-1} \leqslant \Phi_{i,j-\frac{1}{2}} \leqslant \bar{\Phi}_{i,j}, \quad \bar{\Phi}_{i,j} \leqslant \Phi_{i,j+\frac{1}{2}} \leqslant \bar{\Phi}_{i,j+1}. \tag{39b}$$

It is noted that Eq. (39b) does not possess any information on the property distribution at cell vertex points, which would be essential when property gradient is not aligned with grid lines. Thus, as an extended condition of Eq. (39) which includes the missing information, we require Eq. (40) on compact stencil in Fig. 3.

$$\bar{\Phi}^{\min}_{\text{neighbor}} < \Phi < \bar{\Phi}^{\max}_{\text{neighbor}}. \tag{40}$$

Since Eq. (38) does not automatically imply Eq. (40), (38) as well as Eq. (40) has to be satisfied to control oscillations in multi-space dimensions. In order to realize Eq. (40), the values at vertex points, Φ_2, and Φ_4 in Fig. 4, are required to satisfy the following condition:

$$\min\left(\bar{\Phi}_{i,j}, \bar{\Phi}_{i+1,j}, \bar{\Phi}_{i,j-1}, \bar{\Phi}_{i+1,j-1}\right) < \Phi_1 < \max\left(\bar{\Phi}_{i,j}, \bar{\Phi}_{i+1,j}, \bar{\Phi}_{i,j-1}, \bar{\Phi}_{i+1,j-1}\right), \tag{41a}$$

$$\min\left(\bar{\Phi}_{i,j}, \bar{\Phi}_{i+1,j}, \bar{\Phi}_{i,j+1}, \bar{\Phi}_{i+1,j+1}\right) < \Phi_2 < \max\left(\bar{\Phi}_{i,j}, \bar{\Phi}_{i+1,j}, \bar{\Phi}_{i,j+1}, \bar{\Phi}_{i+1,j+1}\right), \tag{41b}$$

$$\min\left(\bar{\Phi}_{i,j}, \bar{\Phi}_{i-1,j}, \bar{\Phi}_{i,j+1}, \bar{\Phi}_{i-1,j+1}\right) < \Phi_3 < \max\left(\bar{\Phi}_{i,j}, \bar{\Phi}_{i-1,j}, \bar{\Phi}_{i,j+1}, \bar{\Phi}_{i-1,j+1}\right), \tag{41c}$$

$$\min\left(\bar{\Phi}_{i,j}, \bar{\Phi}_{i-1,j}, \bar{\Phi}_{i,j-1}, \bar{\Phi}_{i-1,j-1}\right) < \Phi_4 < \max\left(\bar{\Phi}_{i,j}, \bar{\Phi}_{i-1,j}, \bar{\Phi}_{i,j-1}, \bar{\Phi}_{i-1,j-1}\right). \tag{41d}$$

And, a multi-dimensional limiting function which is compatible with Eq. (38) and at the same time yield the distribution of Eq. (41) has to be formulated.

If discontinuity is inclined by $_j$ as in Fig. 4 and $0 < _j < 90°$, Eq. (41) becomes

$$\bar{\Phi}_{i,j-1} < \Phi_1 < \bar{\Phi}_{i+1,j}, \tag{42a}$$

$$\bar{\Phi}_{i,j} < \Phi_2 < \bar{\Phi}_{i+1,j+1}, \tag{42b}$$

$$\bar{\Phi}_{i-1,j} < \Phi_3 < \bar{\Phi}_{i,j+1}, \tag{42c}$$

$$\bar{\Phi}_{i-1,j-1} < \Phi_4 < \bar{\Phi}_{i,j}. \tag{42d}$$

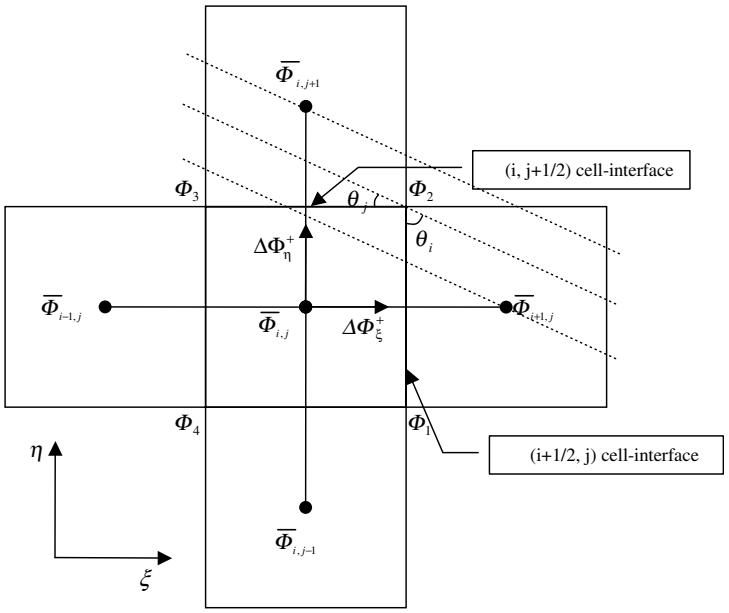

Fig. 4. Distributions of cell averaged values and cell vertex values.

The case of $90° < \ _j < 180°$ is symmetric with respect to $\ = 0$ line, the case of $180° < \ _j < 270°$ is the same as the case of $0° < \ _j < 90°$ and the case of $270° < \ _j < 360°$ is symmetric with respect to $\ = 0$ line. Now, let us consider the values at four vertex points which are evaluated as

$$\boldsymbol{\Phi}_1 = \bar{\boldsymbol{\Phi}}_{i,j} + \Delta\boldsymbol{\Phi}^- + \Delta\boldsymbol{\Phi}^+, \tag{43a}$$

$$\boldsymbol{\Phi}_2 = \bar{\boldsymbol{\Phi}}_{i,j} + \Delta\boldsymbol{\Phi}^+ + \Delta\boldsymbol{\Phi}^+ = \bar{\boldsymbol{\Phi}}_{i,j} + \left(1 + \tan\tilde{\ }_j\right)\Delta\boldsymbol{\Phi}^+, \tag{43b}$$

$$\boldsymbol{\Phi}_3 = \bar{\boldsymbol{\Phi}}_{i,j} + \Delta\boldsymbol{\Phi}^+ + \Delta\boldsymbol{\Phi}^-, \tag{43c}$$

$$\boldsymbol{\Phi}_4 = \bar{\boldsymbol{\Phi}}_{i,j} + \Delta\boldsymbol{\Phi}^- + \Delta\boldsymbol{\Phi}^- = \bar{\boldsymbol{\Phi}}_{i,j} + \left(1 + \tan\tilde{\ }_j\right)\Delta\boldsymbol{\Phi}^-, \tag{43d}$$

where $\tilde{\ }$ is defined as $\tan\tilde{\ }_j = \frac{\Delta\boldsymbol{\Phi}^+}{\Delta\boldsymbol{\Phi}^+}$ in Fig. 4. $\Delta\boldsymbol{\Phi}^\pm_{,}$ are the variations from center point to cell-interface as in Fig. 5. Thus, $\Delta\boldsymbol{\Phi}^\pm$ has an opposite sign with each other: when $0 < \ _j < 90°$, $\Delta\boldsymbol{\Phi}^+$ is positive and $\Delta\boldsymbol{\Phi}^-$ is negative and $\tan\tilde{\ } > 0$.

From Eq. (39), the interpolated value $\boldsymbol{\Phi}_{i,j\pm\frac{1}{2}}$ and $\boldsymbol{\Phi}_{i\pm\frac{1}{2},j}$ should satisfy the following conditions.

$$\bar{\boldsymbol{\Phi}}_{i-1,j} \leqslant \boldsymbol{\Phi}_{i-\frac{1}{2},j} \leqslant \bar{\boldsymbol{\Phi}}_{i,j} \leqslant \boldsymbol{\Phi}_{i+\frac{1}{2},j} \leqslant \bar{\boldsymbol{\Phi}}_{i+1,j}, \tag{44a}$$

$$\bar{\boldsymbol{\Phi}}_{i,j-1} \leqslant \boldsymbol{\Phi}_{i,j-\frac{1}{2}} \leqslant \bar{\boldsymbol{\Phi}}_{i,j} \leqslant \boldsymbol{\Phi}_{i,j+\frac{1}{2}} \leqslant \bar{\boldsymbol{\Phi}}_{i,j+1}, \tag{44b}$$

where $\boldsymbol{\Phi}_{i\pm\frac{1}{2},j} = \bar{\boldsymbol{\Phi}}_{i,j} + \Delta\boldsymbol{\Phi}^\pm$ and $\boldsymbol{\Phi}_{i,j\pm\frac{1}{2}} = \bar{\boldsymbol{\Phi}}_{i,j} + \Delta\boldsymbol{\Phi}^\pm$. From Eqs. (43) and (44), is always greater than $\bar{\boldsymbol{\Phi}}_{i,j-1}$ and less than $\bar{\boldsymbol{\Phi}}_{i+1,j}$ because $\Delta\boldsymbol{\Phi}^+$ is positive and $\Delta\boldsymbol{\Phi}^-$ is negative:

$$\bar{\boldsymbol{\Phi}}_{i,j-1} < \boldsymbol{\Phi}_{i,j-\frac{1}{2}} < \bar{\boldsymbol{\Phi}}_{i,j} + \Delta\boldsymbol{\Phi}^- + \Delta\boldsymbol{\Phi}^+ = \boldsymbol{\Phi}_1 < \boldsymbol{\Phi}_{i+\frac{1}{2},j} < \bar{\boldsymbol{\Phi}}_{i+1,j}. \tag{45a}$$

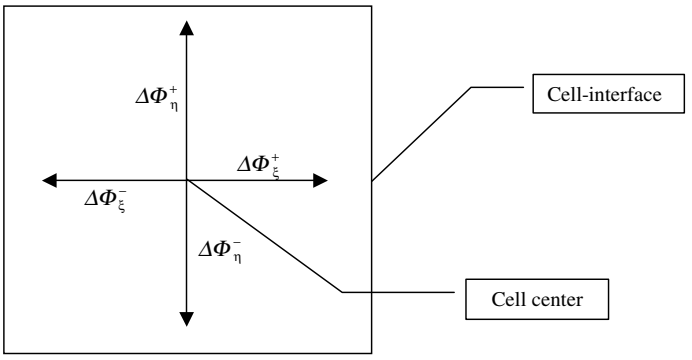

Fig. 5. Definition of property variations within a cell.

Similarly, Φ_3 is always greater than $\bar{\Phi}_{i-1,j}$ and less than $\bar{\Phi}_{i,j+1}$

$$\bar{\Phi}_{i-1,j} < \Phi_{i-\frac{1}{2},j} < \bar{\Phi}_{i,j} + \Delta\Phi^- + \Delta\Phi^+ = \Phi_3 < \Phi_{i,j+\frac{1}{2}} < \bar{\Phi}_{i,j+1}. \tag{45b}$$

Thus, and Φ_3 always satisfy Eqs. (42a) and (42c).

Now, let us check the cases of Φ_2 and Φ_4. In case of Φ_2, from $\bar{\Phi}_{i,j} < \Phi_2 = \bar{\Phi}_{i,j} + \left(1 + \tan\tilde{}_j\right)\Delta\Phi^+$, Eq. (42b) is satisfied only if Φ_2 would be less than $\bar{\Phi}_{i+1,j+1}$.

$$\Phi_2 = \bar{\Phi}_{i,j} + \left(1 + \tan\tilde{}_j\right)\Delta\Phi^+ \leqslant \bar{\Phi}_{i+1,j+1} = \bar{\Phi}_{i,j} + \Delta\Phi_{i,j+\frac{1}{2}} + \Delta\Phi_{i+\frac{1}{2},j+1}. \tag{46}$$

And

$$\Delta\Phi_{i+\frac{1}{2},j+1} = \tan\bar{}_{j+1}\Delta\Phi_{i,j+\frac{3}{2}} = \tan\bar{}_{j+1}\frac{\Delta\Phi_{i,j+\frac{3}{2}}}{\Delta\Phi_{i,j+\frac{1}{2}}}\Delta\Phi_{i,j+\frac{1}{2}} = \frac{\tan\bar{}_{j+1}}{r_{\mathrm{R},j+1}}\Delta\Phi_{i,j+\frac{1}{2}}, \tag{47}$$

where $\bar{}$ is defined as $\tan\bar{}_{j+1} = \frac{\Delta\Phi_{i+\frac{1}{2},j+1}}{\Delta\Phi_{i,j+\frac{3}{2}}}$ and $r_{\mathrm{R},j+1} = \frac{\Delta\Phi_{i,j+\frac{1}{2}}}{\Delta\Phi_{i,j+\frac{3}{2}}}$.

Thus, from Eqs. (46) and (47),

$$\Delta\Phi^+ \leqslant \frac{\left(1 + \frac{\tan\bar{}_{j+1}}{r_{\mathrm{R},j+1}}\right)}{\left(1 + \tan\tilde{}_j\right)}\Delta\Phi_{i,j+\frac{1}{2}}. \tag{48}$$

And, from Eqs. (7) and (38), the maximum variation of $\Delta\Phi^+$ is determined as

$$\Delta\Phi^+ = \Delta\Phi_{i,j-\frac{1}{2}} \quad (r_{\mathrm{L},j} > 1), \quad \Delta\Phi^+ = \Delta\Phi_{i,j+\frac{1}{2}} \quad (0 < r_{\mathrm{L},j} < 1), \tag{49}$$

where $r_{\mathrm{L},j} = \frac{1}{r_{\mathrm{R},j}} = \frac{\Delta\Phi_{i,j+\frac{1}{2}}}{\Delta\Phi_{i,j-\frac{1}{2}}}$. Thus, by limiting the maximum variation of $\Delta\Phi^+$, all of the Eq. (42) can be realized as follows:

When $r_{\mathrm{L},j} > 1$,

The maximum variation is modified as $\Delta\Phi^+ = 0.5\alpha\Delta\Phi_{i,j-\frac{1}{2}}$ instead of $\Delta\Phi^+ = \Delta\Phi_{i,j-\frac{1}{2}}$. Then, from Eq. (48), we can determine the value of $\alpha(1 \leqslant \alpha \leqslant 2)$ which satisfies Eq. (42b).

$$0.5\frac{\alpha}{r_{\mathrm{L},j}}\Delta\Phi_{i,j+\frac{1}{2}} \leqslant \frac{\left(1 + \frac{\tan\bar{}_{j+1}}{r_{\mathrm{R},j+1}}\right)}{\left(1 + \tan\tilde{}_j\right)}\Delta\Phi_{i,j+\frac{1}{2}}, \tag{50a}$$

where $\Delta\Phi^+ = 0.5\alpha\Delta\Phi_{i,j-\frac{1}{2}} = 0.5\frac{\alpha}{r_{\mathrm{L},j}}\Delta\Phi_{i,j+\frac{1}{2}} \quad (1 \leqslant \alpha \leqslant 2)$.

Thus, we have

$$1 \leqslant \alpha \leqslant \min\left[2, \frac{2r_{\mathrm{L},j}\left(1+\frac{\tilde{\tan}_{j+1}}{r_{\mathrm{R},j+1}}\right)}{\left(1+\tilde{\tan}_{j}\right)}\right]. \tag{50b}$$

When $0 < r_{\mathrm{L},j} < 1$,

Similarly, the maximum variation is modified as $\Delta\boldsymbol{\Phi}^{+} = 0.5\alpha\Delta\boldsymbol{\Phi}_{i,j+\frac{1}{2}}$ instead of $\Delta\boldsymbol{\Phi}^{+} = \Delta\boldsymbol{\Phi}_{i,j+\frac{1}{2}}$. By inserting $\Delta\boldsymbol{\Phi}^{+} \leqslant 0.5\alpha\Delta\boldsymbol{\Phi}_{i,j+\frac{1}{2}}$ $(1 \leqslant \alpha \leqslant 2)$ into Eq. (48),

$$0.5\alpha\Delta\boldsymbol{\Phi}_{i,j+\frac{1}{2}} \leqslant \frac{\left(1+\frac{\tilde{\tan}_{j+1}}{r_{\mathrm{R},j+1}}\right)}{\left(1+\tilde{\tan}_{j}\right)}\Delta\boldsymbol{\Phi}_{i,j+\frac{1}{2}}. \tag{51a}$$

Then, we obtain

$$1 \leqslant \alpha \leqslant \min\left[2, \frac{2\left(1+\frac{\tilde{\tan}_{j+1}}{r_{\mathrm{R},j+1}}\right)}{\left(1+\tilde{\tan}_{j}\right)}\right]. \tag{51b}$$

Eqs. (50b) and (51b) always make $\boldsymbol{\Phi}_2$ less than $\bar{\boldsymbol{\Phi}}_{i+1,j+1}$, and Eq. (42b) is realized.

Next, let us consider the case of $r_{\mathrm{R},j+1} < 0$ in Eq. (48). From Eq. (47), it is the case where $\bar{\boldsymbol{\Phi}}_{i+1,j+1}$ is less than $\bar{\boldsymbol{\Phi}}_{i,j+1}$. If the case of $r_{\mathrm{R},j+1} < 0$ is ignored, α is restricted too much and a computed solution can be undesirably diffusive. Thus, the condition, that $\boldsymbol{\Phi}_2$ should be less than $\bar{\boldsymbol{\Phi}}_{i,j+1}$ instead of $\bar{\boldsymbol{\Phi}}_{i+1,j+1}$ when $r_{\mathrm{R},j+1} < 0$, is introduced.

When $r_{\mathrm{R},j+1} < 0$, we require

$$\boldsymbol{\Phi}_2 = \bar{\boldsymbol{\Phi}}_{i,j} + \left(1+\tilde{\tan}_{j}\right)\Delta\boldsymbol{\Phi}^{+} \leqslant \bar{\boldsymbol{\Phi}}_{i,j+1} = \bar{\boldsymbol{\Phi}}_{i,j} + \Delta\boldsymbol{\Phi}_{i,j+\frac{1}{2}}. \tag{52a}$$

Then,

$$\Delta\boldsymbol{\Phi}^{+} \leqslant \frac{1}{\left(1+\tilde{\tan}_{j}\right)}\Delta\boldsymbol{\Phi}_{i,j+\frac{1}{2}}. \tag{52b}$$

Similar to the above procedure, the range of the restriction coefficient α is derived for the following cases.

When $r_{\mathrm{L},j} > 1$ and $r_{\mathrm{R},j+1} < 0$,

$$1 \leqslant \alpha \leqslant \min\left[2, \frac{2r_{\mathrm{L},j}}{\left(1+\tilde{\tan}_{j}\right)}\right]. \tag{53}$$

When $0 < r_{\mathrm{L},j} < 1$ and $r_{\mathrm{R},j+1} < 0$,

$$1 \leqslant \alpha \leqslant \frac{2}{\left(1+\tilde{\tan}_{j}\right)}. \tag{54}$$

Finally, by combining Eqs. (50b), (51b), (53) and (54), the range of α can be formulated as follows:

$$1 \leqslant \alpha \leqslant \min\left[2, \frac{2\max\left(1, r_{\mathrm{L},j}\right)\left(1+\max\left(0, \frac{\tilde{\tan}_{j+1}}{r_{\mathrm{R},j+1}}\right)\right)}{\left(1+\tilde{\tan}_{j}\right)}\right]. \tag{55}$$

Eq. (55) expresses the information of the restriction coefficient α for multi-dimensional monotonicity. If we choose the maximum value of α, the multi-dimensional limiting function is obtained as follows:

The value of α contains two angles related to property variation, $\tilde{}$ and $\bar{}$, defined at each cell. Although $\tilde{}$ and $\bar{}$ are defined separately for the purpose of rigor, the difference is negligible in real computations, which will be shown well through test problems in Section 4. Thus, for computational efficiency we introduce the representative angle, . The analysis on the relation among the three angles ($\tilde{}$, $\bar{}$,) is explained in Section 3.5. From the definition of $\tilde{}$ and $\bar{}$,

$$\tan\tilde{}_j = \frac{\Delta\boldsymbol{\Phi}^+}{\Delta\boldsymbol{\Phi}^+} \text{ and } \tan\bar{}_j = \frac{\Delta\boldsymbol{\Phi}_{i+\frac{1}{2},j}}{\Delta\boldsymbol{\Phi}_{i,j+\frac{1}{2}}}, \tag{56}$$

where $0° < {}_j < 90°$. These are simply the ratios of variations in the and directions defined at each cell.

Similarly, we define the following representative ratio of variation as

$$\tan {}_j = \frac{\left(\bar{\boldsymbol{\Phi}}_{i+1,j} - \bar{\boldsymbol{\Phi}}_{i-1,j}\right)}{\left(\bar{\boldsymbol{\Phi}}_{i,j+1} - \bar{\boldsymbol{\Phi}}_{i,j-1}\right)} > 0. \tag{57}$$

Fig. 6 show the definitions of three angles. When $90° < {}_j < 180°$, the maximum value is $\bar{\boldsymbol{\Phi}}_{i-1,j+1}$ in Fig. 4 with $\Delta\boldsymbol{\Phi}^- > 0$, $\Delta\boldsymbol{\Phi}^+ > 0$. Thus,

$$\tan\tilde{}_j = \frac{\Delta\boldsymbol{\Phi}^-}{\Delta\boldsymbol{\Phi}^+} > 0. \tag{58}$$

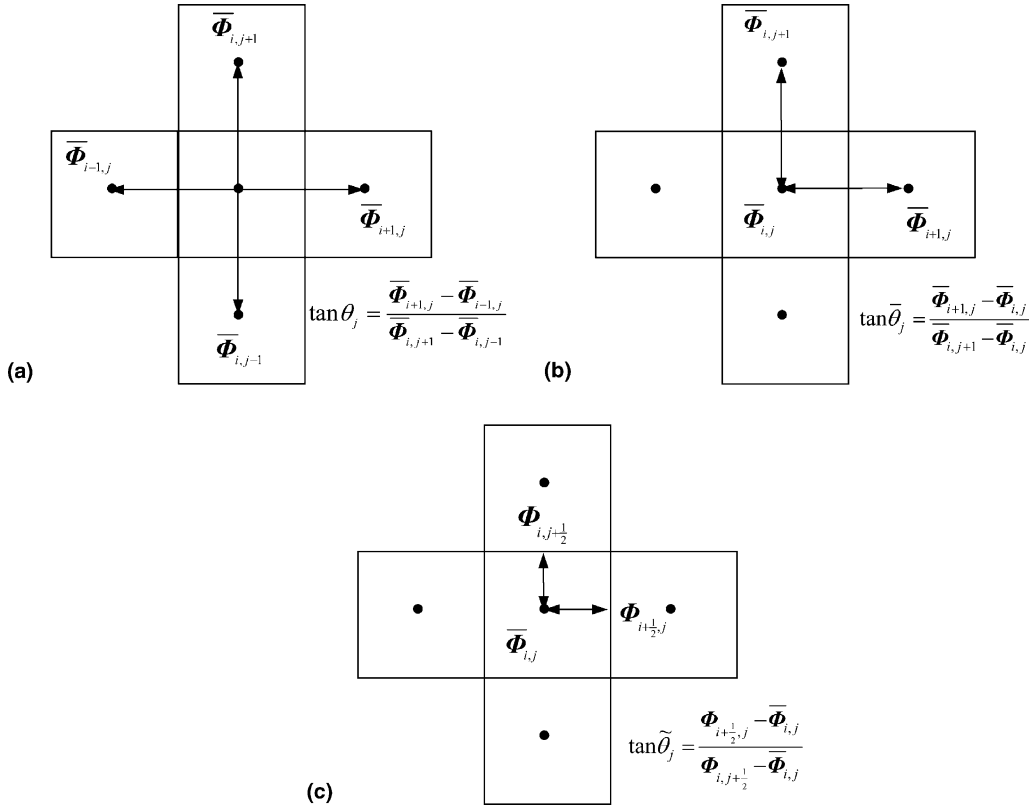

Fig. 6. Definitions of three angles.

In this case, $\tan\ _j$ is written as follows:

$$\tan\ _j = -\frac{\left(\bar{\boldsymbol{\Phi}}_{i+1,j} - \bar{\boldsymbol{\Phi}}_{i-1,j}\right)}{\left(\bar{\boldsymbol{\Phi}}_{i,j+1} - \bar{\boldsymbol{\Phi}}_{i,j-1}\right)} > 0. \tag{59}$$

The cases of $180° < \ _j < 270°$ and $270° < \ _j < 360°$ can be handled in the same way. Finally, we have the following expression for the representative angle

$$\tan\ _j = \left|\frac{\left(\bar{\boldsymbol{\Phi}}_{i+1,j} - \bar{\boldsymbol{\Phi}}_{i-1,j}\right)}{\left(\bar{\boldsymbol{\Phi}}_{i,j+1} - \bar{\boldsymbol{\Phi}}_{i,j-1}\right)}\right|. \tag{60}$$

As a consequence, the one-dimensional limiting condition and the multi-dimensional limiting function are compared as follows:

One-dimensional limiting condition:

$$\max(0, \min(2r, 2)). \tag{61}$$

Multi-dimensional limiting function:

$$\max(0, \min(\alpha r, \alpha)). \tag{62}$$

$\boldsymbol{\Phi}_4$ requires the same condition.

3.3.2. General form of multi-dimensional limiting process (MLP)

With the multi-dimensional limiting function of Eq. (62), a new family of interpolation scheme to control oscillations in a multi-dimensional flow can be developed.

$$\boldsymbol{\Phi}_{\mathrm{L}} = \bar{\boldsymbol{\Phi}}_i + 0.5\phi(r_{\mathrm{L},i}, \alpha_{\mathrm{L}}, \beta_{\mathrm{L}})\Delta\boldsymbol{\Phi}_{i-\frac{1}{2}} = \bar{\boldsymbol{\Phi}}_i + 0.5\max(0, \min(\alpha_{\mathrm{L}} r_{\mathrm{L},i}, \alpha_{\mathrm{L}}, \beta_{\mathrm{L}}))\Delta\boldsymbol{\Phi}_{i-\frac{1}{2}}, \tag{63a}$$

$$\boldsymbol{\Phi}_{\mathrm{R}} = \bar{\boldsymbol{\Phi}}_{i+1} - 0.5\phi(r_{\mathrm{R},i+1}, \alpha_{\mathrm{R}}, \beta_{\mathrm{R}})\Delta\boldsymbol{\Phi}_{i+\frac{3}{2}} = \bar{\boldsymbol{\Phi}}_{i+1} - 0.5\max(0, \min(\alpha_{\mathrm{R}} r_{\mathrm{R},i+1}, \alpha_{\mathrm{R}}, \beta_{\mathrm{R}}))\Delta\boldsymbol{\Phi}_{i+\frac{3}{2}}. \tag{63b}$$

The interpolated values of $\boldsymbol{\Phi}_{\mathrm{L}}$ and $\boldsymbol{\Phi}_{\mathrm{R}}$ are based on the final form of MLP. By inserting Eq. (63) into Eqs. (4) and (5), MLP combined with M-AUSMPW+ are constructed. Other numerical flux can be employed similarly.

Values of $\alpha_{\mathrm{L,R}}$ and $\beta_{\mathrm{L,R}}$ in Eq. (63) is summarized as follows:

Along the -direction,

$$\alpha_{\mathrm{L}} = g\left[\frac{2\max(1, r_{\mathrm{L},i})\left(1 + \max\left(0, \frac{\tan\ _{i+1}}{r_{\mathrm{R},i+1}}\right)\right)}{1 + \tan\ _i}\right], \quad \alpha_{\mathrm{R}} = g\left[\frac{2\max(1, r_{\mathrm{R},i+1})\left(1 + \max\left(0, \frac{\tan\ _i}{r_{\mathrm{L},i}}\right)\right)}{1 + \tan\ _{i+1}}\right], \tag{64a}$$

where $r_{\mathrm{L},i} = \frac{\Delta\boldsymbol{\Phi}_{i+\frac{1}{2},j}}{\Delta\boldsymbol{\Phi}_{i-\frac{1}{2},j}}$, $r_{\mathrm{R},i+1} = \frac{\Delta\boldsymbol{\Phi}_{i+\frac{1}{2},j}}{\Delta\boldsymbol{\Phi}_{i+\frac{3}{2},j}}$ and $g(x) = \max(1,\min(2,x))$.

Along the -direction,

$$\alpha_{\mathrm{L}} = g\left[\frac{2\max(1, r_{\mathrm{L},j})\left(1 + \max\left(0, \frac{\tan\ _{j+1}}{r_{\mathrm{R},j+1}}\right)\right)}{1 + \tan\ _j}\right], \quad \alpha_{\mathrm{R}} = g\left[\frac{2\max(1, r_{\mathrm{R},j+1})\left(1 + \max\left(0, \frac{\tan\ _j}{r_{\mathrm{L},j}}\right)\right)}{1 + \tan\ _{j+1}}\right], \tag{64b}$$

where $r_{\mathrm{L},j} = \frac{\Delta\boldsymbol{\Phi}_{i,j+\frac{1}{2}}}{\Delta\boldsymbol{\Phi}_{i,j-\frac{1}{2}}}$, $r_{\mathrm{R},j+1} = \frac{\Delta\boldsymbol{\Phi}_{i,j+\frac{1}{2}}}{\Delta\boldsymbol{\Phi}_{i,j+\frac{3}{2}}}$ and

$$\tan\ _i = \left|\frac{\left(\bar{\Phi}_{i,j+1} - \bar{\Phi}_{i,j-1}\right)}{\left(\bar{\Phi}_{i+1,j} - \bar{\Phi}_{i-1,j}\right)}\right|, \quad \tan\ _j = \left|\frac{\left(\bar{\Phi}_{i+1,j} - \bar{\Phi}_{i-1,j}\right)}{\left(\bar{\Phi}_{i,j+1} - \bar{\Phi}_{i,j-1}\right)}\right|.$$

Combining Eqs. (63) and (64) with Eqs. (33) and (37) for β, we finally obtain MLP3, MLP5.

MLP with third order interpolation (MLP3):

$$\beta_L = \frac{1 + 2r_{L,i}}{3}, \quad \beta_R = \frac{1 + 2r_{R,i+1}}{3}. \tag{65a}$$

MLP with fifth order interpolation (MLP5):

$$\beta_L = \frac{-2/r_{L,i-1} + 11 + 24r_{L,i} - 3r_{L,i}r_{L,i+1}}{30}, \tag{65b}$$

$$\beta_R = \frac{-2/r_{R,i+2} + 11 + 24r_{R,i+1} - 3r_{R,i+1}r_{R,i}}{30}. \tag{65c}$$

3.4. Comparison between MLP and TVD limiters

To compare MLP with several TVD limiters, all of the limiters are re-written by the β parameter form as

$$\phi = \max(0, \min(\beta_1 r, 1), \min(r, \beta_2)), \tag{66}$$

with $1 < \beta_1,\ \beta_2 < 2$.

Let us assume some interpolation function $f(r)$ is given within second order TVD region. When $0 < r < 1$, $f(r)$ should be within the region A in Fig. 7.

$$r < f(r) < 2r \quad \text{and} \quad f(r) < 1. \tag{67}$$

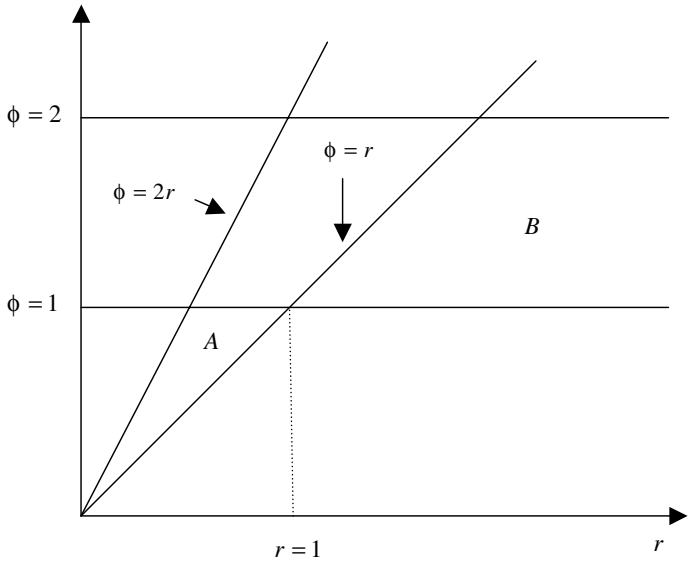

Fig. 7. TVD limiter region.

In the β limiter form, it corresponds to

$$\phi = (0, \min(\beta_1 r, 1), r) = \min(\beta_1 r, 1). \tag{68}$$

Then, by defining, $\beta_1 = \min(2, \max(\frac{f(r)}{r}, 1))$, Eqs. (67) and (68) are equivalent.

When $1 < r$, $f(r)$ lies within the region B in Fig. 7.

$$1 < f(r) < 2 \quad \text{and} \quad f(r) < r. \tag{69}$$

And in the β limiter form, it is

$$\phi = \max(0, 1, \min(r, \beta_2)) = \min(r, \beta_2). \tag{70}$$

Then, Eqs. (69) and (70) are equivalent with $\beta_2 = \min(2, \max(f(r),1))$. By combining Eqs. (68) and (70), the β limiter form with $f(r)$ can be expressed as follows:

$$\phi = \max(0, \min(\beta_1 r, 1), \min(r, \beta_2)), \tag{71}$$

where $\beta_1 = \min(2, \max(\frac{f(r)}{r}, 1))$ and $\beta_2 = \min(2, \max(f(r), 1))$.

Thus, if the multi-dimensional limiting function is applied to Eq. (72), we obtain the multi-dimensional β limiter form as

$$\phi = \max(0, \min(\beta_1 r, 1), \min(r, \beta_2)), \tag{72}$$

where $\beta_1 = \min(\alpha, \max(\frac{f(r)}{r}, 1))$ and $\beta_2 = \min(\alpha, \max(f(r),1))$.

Exploiting Eq. (72), TVD limiters with the multi-dimensional limiting function can be derived as follows:

MLP with minmod limiter:

$$\phi = \max(0, \min(\beta_1 r, 1), \min(r, \beta_2)), \tag{73a}$$

where $\beta_1 = \beta_2 = 1$. It is seen that the multi-dimensional minmod limiter is exactly the same as the original minmod limiter of Eq. (8). It means that the original minmod limiter maintains monotonic property in multi-dimensional flows.

MLP with van Leer limiter:

$$\phi = \max[0, \min(\alpha, \alpha r, f(r))], \tag{73b}$$

where $f(r) = \frac{2r}{1+r}$.

MLP with superbee limiter:

$$\phi = \max(0, \min(\alpha r, 1), \min(r, \alpha)). \tag{73c}$$

MLP with third order interpolation (MLP3):

$$\phi = \max[0, \min(\alpha, \alpha r, f(r))], \tag{73d}$$

where $f(r) = \frac{1+2r}{3}$.

MLP with fifth order interpolation (MLP5):

$$\phi = \max[0, \min(\alpha, \alpha r, f(r))], \tag{73e}$$

where $f(r) = \frac{-2/r_{i-1}+11+24r_i-3r_i r_{i+1}}{30}$.

Fig. 8 shows several limiting functions including minmod, van Leer, superbee limiter and third order interpolation with TVD limiting. Those are the results without imposing the multi-dimensional effect, i.e., $\alpha = 2$. Fig. 9 is the region of MLP-van Leer, MLP-superbee limiter and MLP3. It is shown that MLP region is completely within the one-dimensional TVD limiting condition because the value of α is always between one and two.

Although α in the multi-dimensional limiting function is the complicated function of r_L, r_R, $_{i \text{ or } j}$ and $_{i+1 \text{ or } j+1}$, it can be roughly compared with TVD limiters by simplifying the property distribution as $\frac{1}{r_R} \approx r_L \approx r$ and $_i \approx$ $_{i+1}$ on regular mesh. Then, the value of becomes

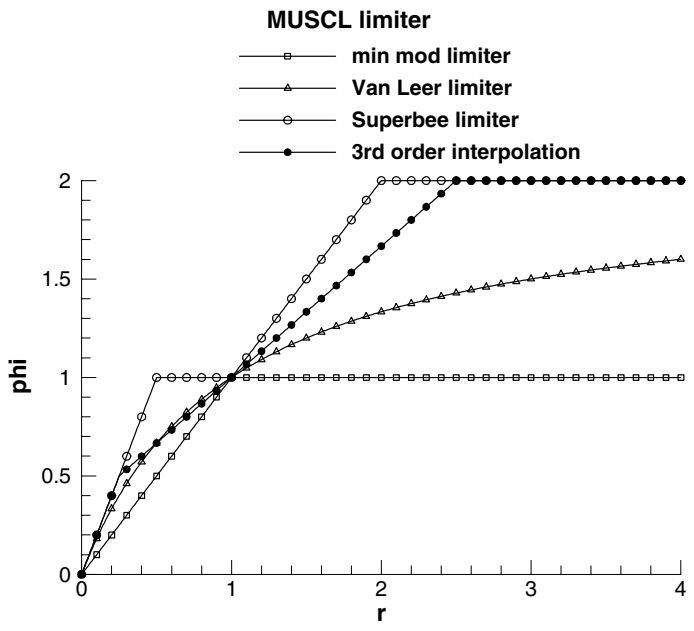

Fig. 8. TVD limiters without multi-dimensional effect.

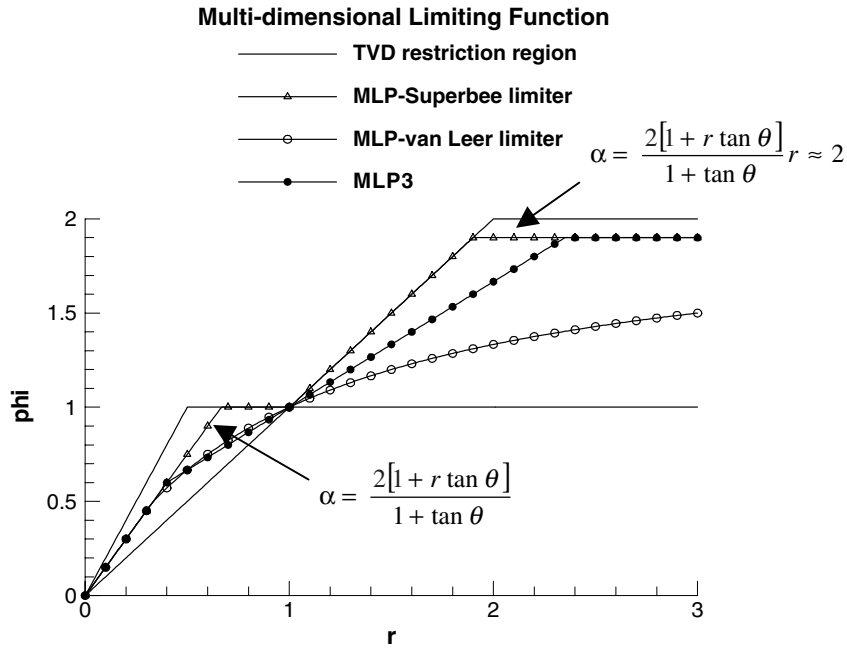

Fig. 9. Comparison of several MLPs.

When $0 < \frac{1}{r_R} < r_L < 1$,

$$1 < \alpha \approx \frac{2(1 + r\tan\ )}{1 + \tan} < 2. \tag{74a}$$

When $\frac{1}{r_R} > r_L > 1$,

$$\alpha \approx \max\left(2, \frac{2r(1 + r\tan\ )}{1 + \tan}\right) = 2. \tag{74b}$$

In discontinuous region of ($r \ll 1$), when is zero, *i.e.*, the local one-dimensional assumption is readily acceptable, the value of becomes two irrespective of *r,* which is identical to the range of superbee limiter. When $\to 45°$, the value of becomes one, which is identical to the range of minmod limiter. As a result, the excessively steep slope based on one-dimensional flow assumption is restricted and oscillations across a multi-dimensional discontinuity are controlled. On the other hand, in discontinuous region of ($r \gg 1$), the value of becomes two regardless of and *r*.

In smooth region, *r* is nearly one, i.e., $\frac{1}{r_R} \approx r_L \approx 1$ and α becomes nearly two regardless of . Since $f(r) \approx 1 (r \approx 1)$, the limiter function reduces to

$$\phi \approx \max[0, \min(2, 2r, f)] = f. \tag{75}$$

This indicates that MLP3 and MLP5 can recover the fully third and fifth order spatial accuracy in smooth region except for local extrema.

3.5. Relation among gradient angles , ¯ and ˜

In the derivation of α, two angles, ¯ and ˜ are involved. ¯ is the ratio of the variation in the direction to the variation in the direction, i.e., $\bar{\Phi}_{i,j+1} - \bar{\Phi}_{i,j}$ and $\bar{\Phi}_{i+1,j} - \bar{\Phi}_{i,j}$. And, ˜ is the angle based on the variation of $\Phi_{i+\frac{1}{2},j} - \bar{\Phi}_{i,j}$ and $\Phi_{i,j+\frac{1}{2}} - \bar{\Phi}_{i,j}$, where $\Phi_{i+\frac{1}{2},j}$ and $\Phi_{i,j+\frac{1}{2}}$ are cell-interface values. In real computations, these angles are replaced by the representative angle of is introduced for computational efficiency.

Let us consider $0 <$ $< 90°$. Then, on equal spacing regular mesh, three angles are written as follows:

$$= \tan^{-1}\left(\frac{\bar{\Phi}_{i,j+1} - \bar{\Phi}_{i,j-1}}{\bar{\Phi}_{i+1,j} - \bar{\Phi}_{i-1,j}}\right), \tag{76a}$$

$$\bar{} = \tan^{-1}\left(\frac{\bar{\Phi}_{i,j+1} - \bar{\Phi}_{i,j}}{\bar{\Phi}_{i+1,j} - \bar{\Phi}_{i,j}}\right), \tag{76b}$$

$$\tilde{} = \tan^{-1}\left(\frac{\Phi_{i,j+\frac{1}{2}} - \bar{\Phi}_{i,j}}{\Phi_{i+\frac{1}{2},j} - \bar{\Phi}_{i,j}}\right) = \tan^{-1}\left(\frac{\phi(r_{L,j})}{\phi(r_{L,i})}\frac{(\bar{\Phi}_{i,j} - \bar{\Phi}_{i,j-1})}{(\bar{\Phi}_{i,j} - \bar{\Phi}_{i-1,j})}\right), \tag{76c}$$

where $r_{L,i} = \frac{\bar{\Phi}_{i+1,j} - \bar{\Phi}_{i,j}}{\bar{\Phi}_{i,j} - \bar{\Phi}_{i-1,j}}$, $r_{L,j} = \frac{\bar{\Phi}_{i,j+1} - \bar{\Phi}_{i,j}}{\bar{\Phi}_{i,j} - \bar{\Phi}_{i,j-1}}$.

In smooth region, i.e., $r_{L,i} \approx 1$ and $r_{L,j} \approx 1$, $\phi(r_{L,i}) \approx \phi(r_{L,j}) \approx 1$ and $\bar{\Phi}_{i+1,j} - \bar{\Phi}_{i,j} \approx \bar{\Phi}_{i,j} - \bar{\Phi}_{i-1,j} \approx 0.5(\bar{\Phi}_{i+1,j} - \bar{\Phi}_{i-1,j})$. Also, $\bar{\Phi}_{i,j+1} - \bar{\Phi}_{i,j} \approx \bar{\Phi}_{i,j} - \bar{\Phi}_{i,j-1} \approx 0.5(\bar{\Phi}_{i,j+1} - \bar{\Phi}_{i,j-1})$. Then, three angles are equivalent with one another (≈ ≈).

In discontinuous region, let us consider the case of one planar wave. Then,

$$r_{L,i} = r_{L,j} \quad \text{and} \quad \phi(r_{L,i}) = \phi(r_{L,j}), \tag{77a}$$

$$\bar{\Phi}_{i+1,j} - \bar{\Phi}_{i-1,j} = \left(1 + \frac{1}{r_{L,i}}\right)(\bar{\Phi}_{i+1,j} - \bar{\Phi}_{i,j}) = (1 + r_{L,i})(\bar{\Phi}_{i,j} - \bar{\Phi}_{i-1,j}), \tag{77b}$$

$$\bar{\boldsymbol{\Phi}}_{i,j+1} - \bar{\boldsymbol{\Phi}}_{i,j-1} = \left(1 + \frac{1}{r_{\mathrm{L},j}}\right)\left(\bar{\boldsymbol{\Phi}}_{i,j+1} - \bar{\boldsymbol{\Phi}}_{i,j}\right) = \left(1 + r_{\mathrm{L},j}\right)\left(\bar{\boldsymbol{\Phi}}_{i,j} - \bar{\boldsymbol{\Phi}}_{i,j-1}\right). \tag{77c}$$

As a result, all the three angles are equal ($= \tilde{} = \bar{}$).

In other complicated flows, there may be some minor difference among three angles. Through numerous test cases, however, the difference turns out to be negligible in determining α. Even for a shock interaction problem, MLP is shown to control oscillations robustly, which will be verified in Section 4.

3.6. Efficiency and convergence characteristics

Table 1 shows efficiency comparison between MLP and conventional TVD limiter. Considering interpolation routine only (see Table 1a), MLP takes about 3 times more expensive than van Leer limiter. This is mainly due to additional computational cost for α and tan in Eq. (64). However, MLP is much more efficient than popular flux function routine. Thus, as shown in Table 1b, MLP with numerical flux takes about 1.67 times more expensive than TVD schemes. In actual computations, depending on the choice of time integration scheme, the overall elapsed time ratio is about 1.15 only (see Table 1c) which is the result combined with AF-ADI time integration. Therefore, MLP is computationally very competitive to conventional TVD approach.

Computational efficiency is one of the advantages of MLP compared with other higher order interpolation schemes such as ENO-type schemes. It is generally known that ENO/WENO requires much more computational cost than conventional TVD approach. This is because variable stencil is adopted to prevent oscillatory behaviors and occasionally ENO/WENO requires the process to transform primitive or conservative variables into characteristic variables. On the other hand, MLP is very simple to be implemented because it uses the fixed stencil and controls oscillations by simple limiting function. Moreover, MLP is very efficient since its convergence characteristics are especially robust in problems including multi-dimensional physical discontinuities, which will be shown in Section 4. This is very desirable in real applications since it

Table 1a
Efficiency comparison of MLP (interpolation only)

Interpolation only	van Leer limiter	MLP3	MLP5
$\mathrm{Time/time_{VAN}}$	1	2.47	2.96

Table 1b
Efficiency comparison of MLP (interpolation and flux function)

Interpolation + flux function	van Leer limiter + Roe's FDS	MLP3 + Roe's FDS	MLP5 + Roe's FDS	MLP5 + M-AUSMPW+
$\mathrm{Time/time_{VAN\ +\ ROE}}$	1	1.50	1.67	2.05

Table 1c
Efficiency comparison of MLP (overall elapsed time)

Overall time	van Leer limiter + Roe's FDS + AF-ADI	MLP3 + Roe's FDS + AF-ADI	MLP5 + Roe's FDS + AF-ADI	MLP5 + M-AUSMPW+ + AF-ADI
$\mathrm{Time/time_{VAN\ +\ ROE}}$	1	1.12	1.15	1.24

can reduce the overall analysis and/or design time. Even in unsteady cases, robust convergence reduces overall computational cost if dual time stepping method is employed.

4. Numerical results

In order to investigate the actual performance of MLP, several test cases are carried out. They include oblique stationary contact discontinuity, shock wave reflection, expansion fan, vortex flow, shock-wave/boundary-layer interaction, double Mach reflection, shock wave/vortex flow interaction and viscous shock tube problems. Computed results by M-AUSMPW+ (Part I) combined with MLP (Part II) are compared with AUSMPW+ or Roe's FDS with TVD limiter. Occasionally, Roe's FDS with MLP and several TVD limiters are also compared. Since MLP is just an interpolation method independent of spatial discretization schemes, any numerical flux function can be essentially adopted. AF-ADI or LU-SGS is used for the time integration. Dual time stepping method or third order TVD Runge–Kutta time integration [14] is used for unsteady calculation.

For boundary conditions, free stream values are specified as inflow conditions, and extrapolation from the inner computational domain is used for outflow condition. At wall, no-slip condition is specified for velocity, and adiabatic or constant condition is used for wall temperature.

4.1. Oblique stationary contact discontinuity

In order to examine the influence of numerical dissipation when discontinuity is inclined to a cell-interface, oblique contact discontinuity is considered. This test case is also closely related to the accuracy of boundary layer, separated flow or vortex flow.

The initial conditions are as follows:

$$(\ _{\mathrm{L}}, u_{\mathrm{L}}, v_{\mathrm{L}}, p_{\mathrm{L}}) = (2.0, 0.1, 0.1\tan\ \ , 0.714) \quad \text{and} \quad (\ _{\mathrm{R}}, u_{\mathrm{R}}, v_{\mathrm{R}}, p_{\mathrm{R}}) = (1.0, 0.1, 0.1\tan\ \ , 0.714).$$

The initial distribution is inclined by degree angle to a cell-interface as shown in Fig. 10. The grid system is 60×50. Boundary values along the left end and the bottom are fixed as initial conditions. Other sides are extrapolated from the inside.

Fig. 11 shows the comparison of density distribution with 45° angle and Fig. 12 is the case for 60° angle. The results of MLP3 and MLP5 are combined with M-AUSMPW+, and second order TVD schemes with various limiters is calculated by the original Roe's FDS. TVD with van Leer limiter is so diffusive that it seems to be inappropriate in pure multi-dimensional flows. On the other hand, MLP3 and MLP5 yield almost the same results as MLP-supeprbee limiter, which gives the steepest result within the region of the multi-dimensional limiting function of Eq. (62). Although superbee limiter can provide monotonic and a most accurate contact discontinuity as shown in Fig. 11, it can not guarantee the same performance in other cases, especially non-linear system equations. Density distribution using van Leer limiter is captured through 10 cells. MLP with M-AUSMPW+ yields the same result with six cell-interfaces.

4.2. Double shock refection

The free stream Mach number is two and the deflection angle of the lower wall is 15° angle. The grid system is 100×30. Slip boundary condition is applied on the upper and lower walls, and all physical values at the exit are extrapolated. This test problem shows the advantages of MLP clearly in terms of monotonicity and convergence.

Figs. 13 and 14 are the comparisons of pressure distribution of superbee, MLP-superbee limiters, MLP3 and MLP5. The original superbee limiters exhibits pressure oscillations across the oblique shock and does

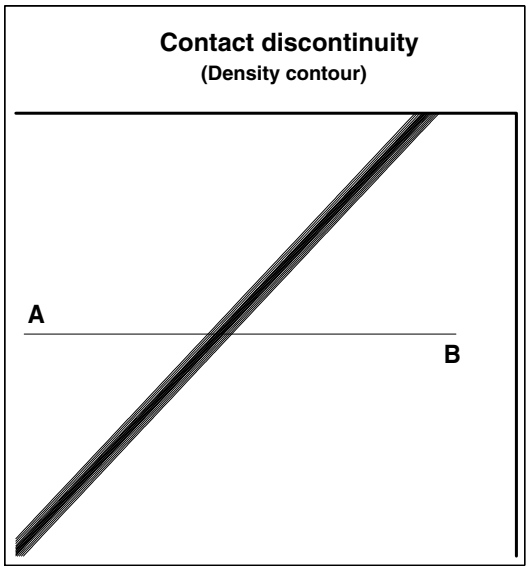

Fig. 10. Discontinuity inclined to a cell-interface by 45° angle.

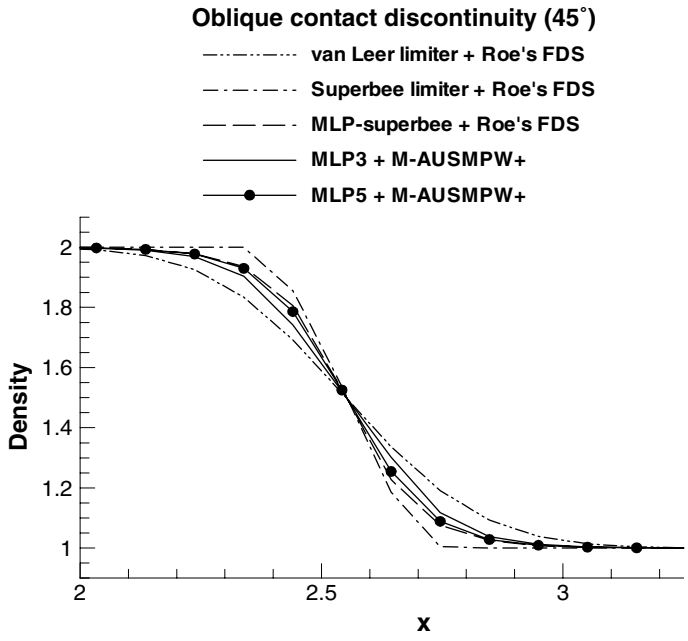

Fig. 11. Density distributions across oblique contact discontinuity (45°).

not maintain a monotonic profile as shown in Figs. 15 and 16. The result by van Leer limiter also shows similar overshoot phenomenon. On the other hand, MLP-superbee limiter provides the best result in maintaining a monotonic shock distribution. MLP3 and MLP5 also do not show overshoot phenomenon and yield

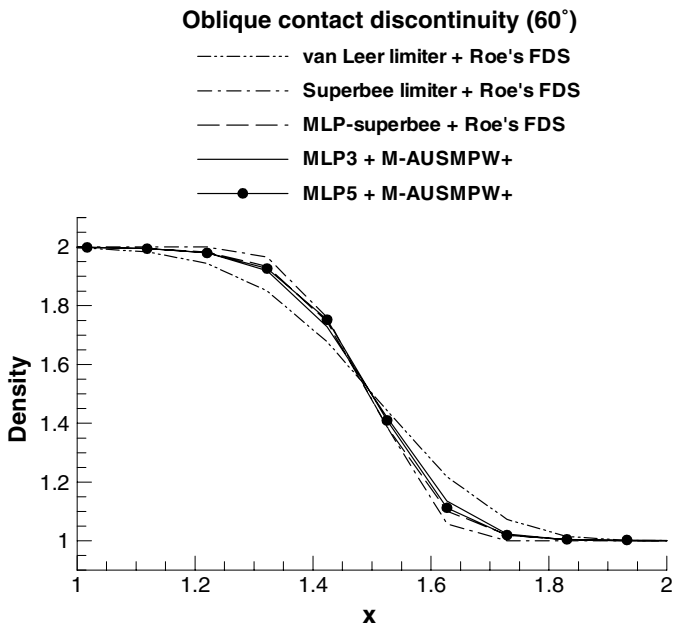

Fig. 12. Density distributions across oblique contact discontinuity (60°).

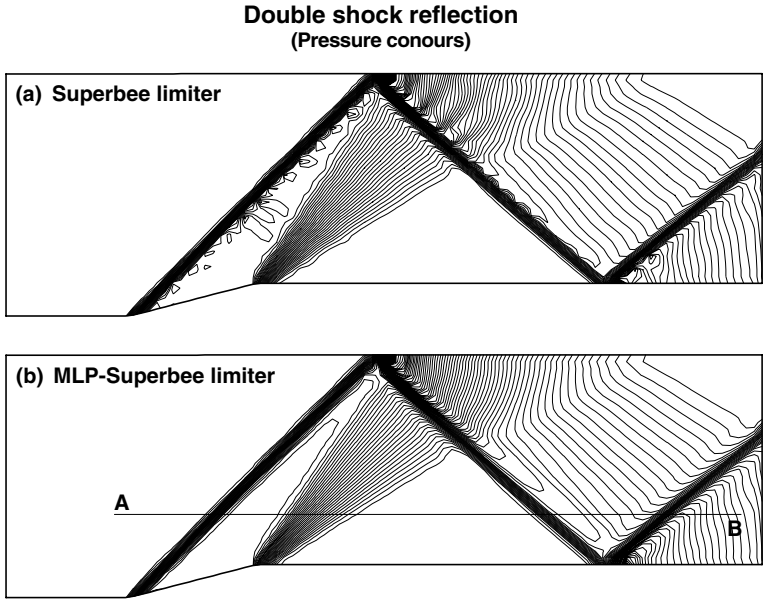

Fig. 13. Comparison of pressure contours (superbee and MLP-superbee limiters).

almost the same accuracy as MLP-superbee limiter. At a glance, MLP-superbee limiter gives the best monotonic result across physical discontinuities. However, it shares the same defect of the original superbee limiter in a sense that entropy decreases in a continuous expansion flow, which is examined in the next test case.

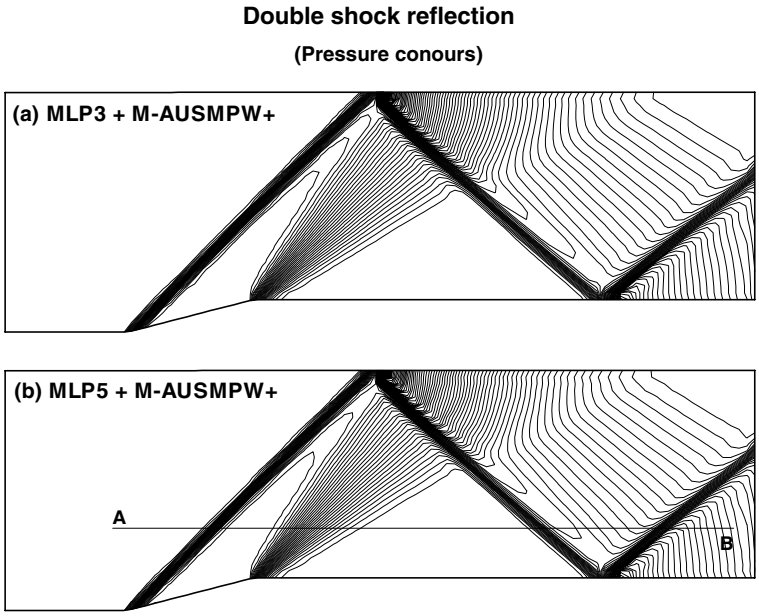

Fig. 14. Comparison of pressure contours (MLP3 and MLP5).

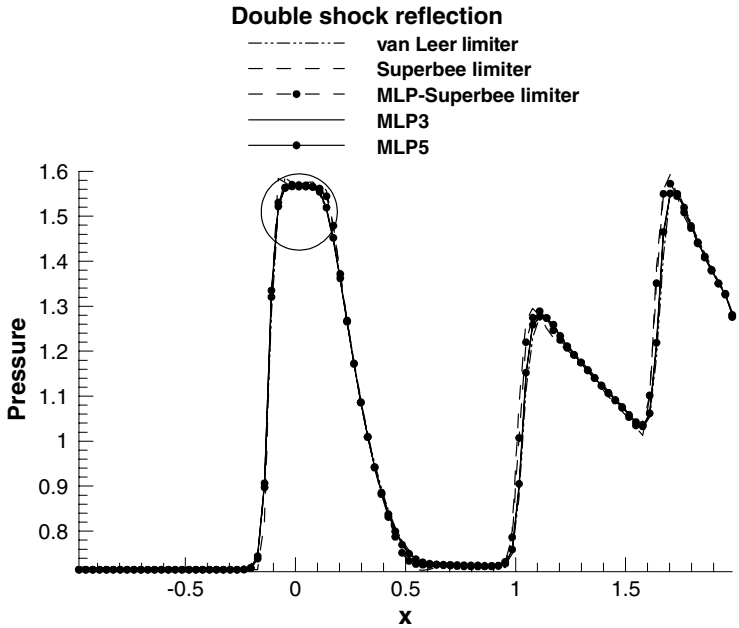

Fig. 15. Comparison of pressure distributions along the line AB.

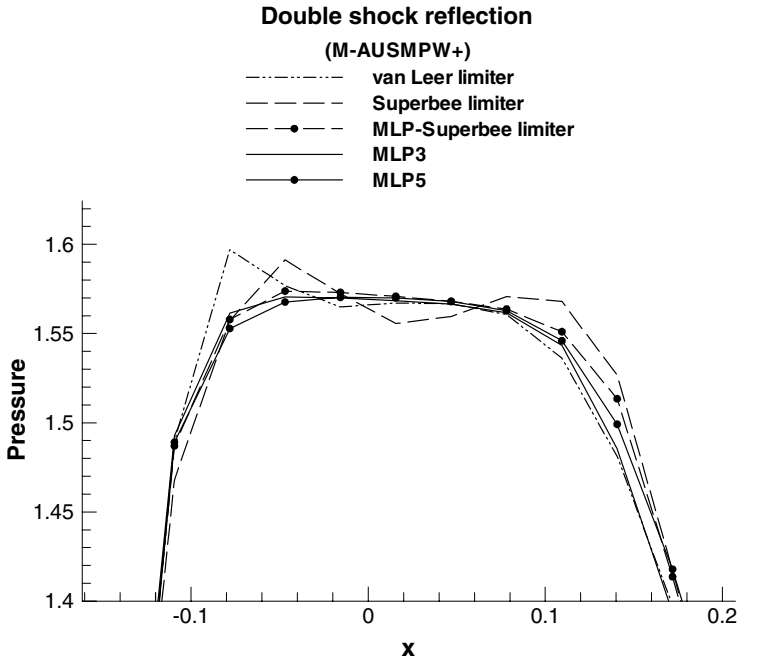

Fig. 16. Comparison of pressure distributions in circle region.

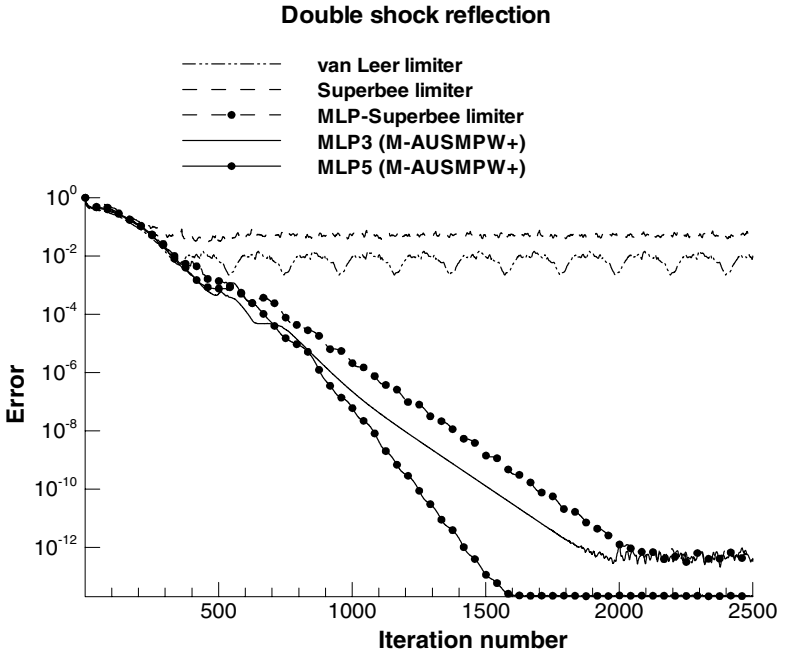

Fig. 17. Error history of double shock reflection.

Fig. 17 shows the error history. CFL number is 3.0 and LU-SGS is used for time integration. Even if the test case is simple, superbee and van Leer limiters are never converged due to oscillatory behavior across the oblique shock discontinuity. On the other hand, MLP-superbee limiter, MLP3 and MLP5 show good convergence characteristics.

4.3. Expansion fan

In this test problem, we examine entropy variation depending on several interpolation schemes. As explained in Section 3.1, the slope of physical distribution is always between the slopes calculated by minmod and superbee limiter. The most important is whether we can estimate the optimal slope or not.

From the analysis of Section 3.1, it is obtained that the slope obtained by minmod limiter is gentler than the physical slope so that a flow becomes more diffusive, i.e., entropy increases excessively, and the slope by superbee limiter is steeper so that entropy decreases unacceptably. Here, it is validated numerically.

The free stream Mach number is two and the wall is deflected by 45° angle. The grid system is 110×80. Slip wall boundary condition is applied and all physical values at the exit are extrapolated. Figs. 18 and 19 are the pressure contour and entropy distribution along a streamline. Entropy for a calorically perfect gas is obtained as follows and the value of s/R is plotted in Fig. 19.

$$s = \frac{\gamma}{\gamma - 1} R \ln T - R \ln P + s_0. \tag{78}$$

The entropy of superbee and MLP-superbee limiter is certainly decreasing while MLP3 and MLP5 give slightly positive entropy variations. As expected, TVD with van Leer limiter yields the largest entropy increase and MLP5 gives the smallest. In this test case, the negative entropy variation due to superbee or MLP-superbee limiter is somewhat bounded and thus it does not cause severe stability problem. However, other cases such as a vortex flow, may lead to serious numerical instability in some problem, which is shown in the next section.

Fig. 20 shows the error history. The results by superbee and MLP-superbee limiter are not converged sufficiently. On the other hand, MLP3 and MLP5 show good convergence characteristics. This is consistent with the entropy variation of each scheme in Fig. 19.

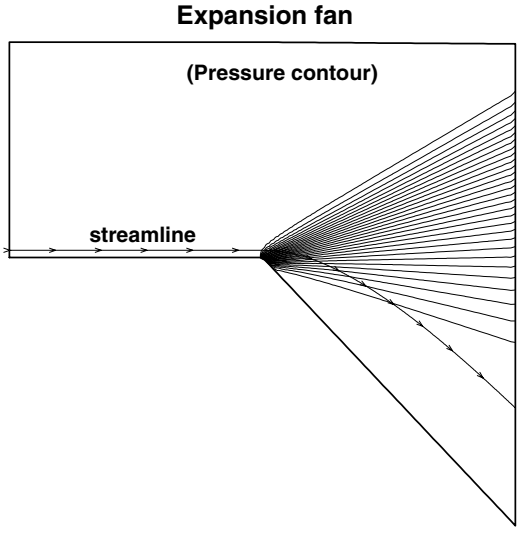

Fig. 18. Pressure contour of expansion fan.

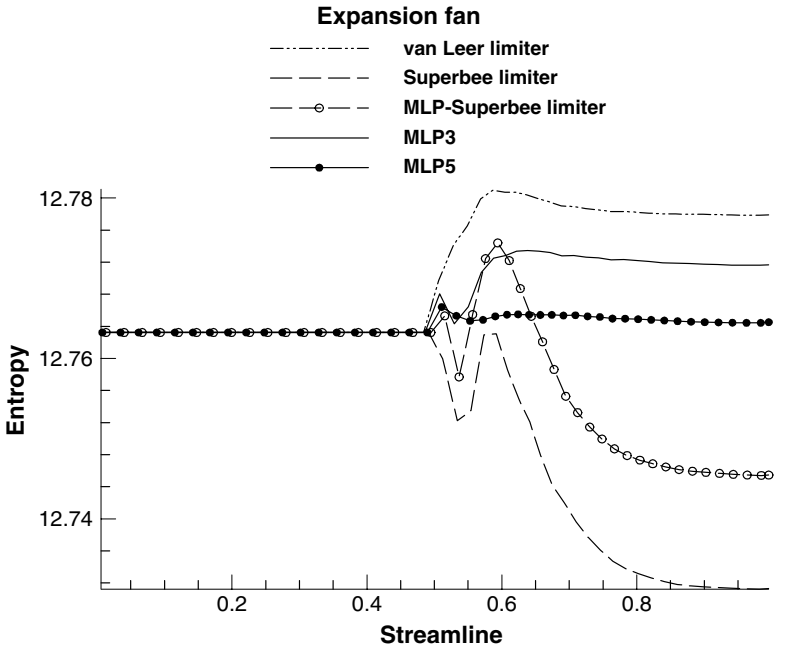

Fig. 19. Entropy variations along the streamline.

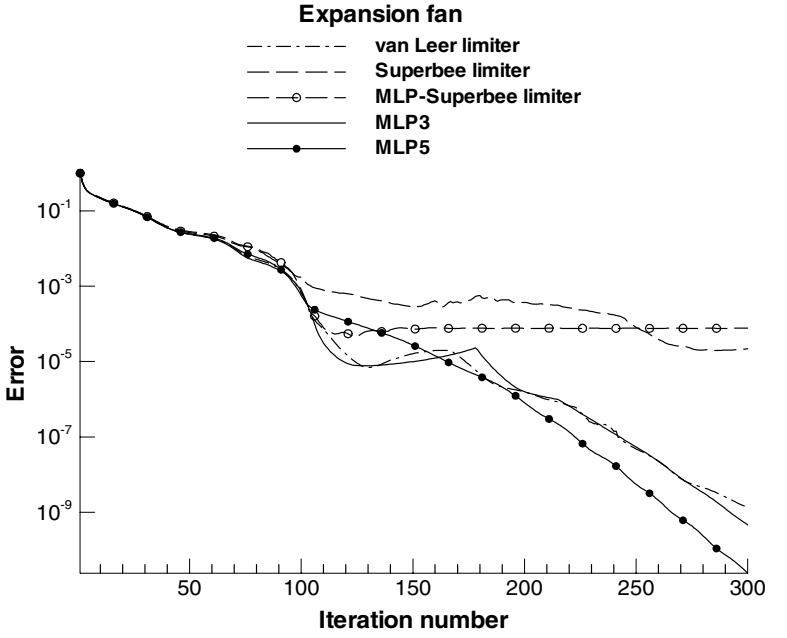

Fig. 20. Error history of several interpolation schemes.

4.4. Stationary vortex flow

It is relatively amenable to improve the accuracy of problems involving physical discontinuities only since the steeper variation always leads to the better result. On the other hand, in continuous flow, optimal variation is definitely necessary. To improve the accuracy of a vortex flow is one of the main objectives in the present paper since it is a good example of multi-dimensional continuous flows. If MLP is very prospective interpolation scheme both in discontinuous and continuous region, it should provide substantially enhanced results in vortex flows.

A vortex flow is a pure multi-dimensional phenomenon, characterized by the existence of negative pressure gradient toward core and the curved flow contours. A flow-aligned grid system is almost impossible in general cases and computed results are very sensitive to the choice of an interpolation and/or numerical fluxes.

Fig. 21 shows the typical computed result. It is Thomson–Rankine vortex model which is composed of the free vortex outside the core and the forced vortex inside.

(a) Free vortex (outside the core):

$$V \cdot r = \text{const} \quad \text{and} \quad \frac{1}{\rho}\frac{\partial p}{\partial r} = \frac{V^2}{r}. \tag{79a}$$

(b) Forced vortex (inside the core):

$$V = \vec{\omega} \cdot r \quad \text{and} \quad \frac{\mathrm{d}p}{\mathrm{d}r} = \rho\frac{V^2}{r}. \tag{79b}$$

Angular velocity $\vec{\omega}$ is 2 and core radius is 0.2. Maximum velocity is $0.36c_\infty$. Computational domain is from -2 to 2 with equal spacing. For grid convergence test, 25×25, 50×50, 75×75 and 100×100 grid points are employed. Roe's FDS, AUSMPW+ and M-AUSMPW+ are used for numerical fluxes and third order TVD Runge–Kutta time integration method is used. CFL number is 0.8 and boundary is fixed as initial values. The pressure distributions are plotted at the non-dimensional time of 40.

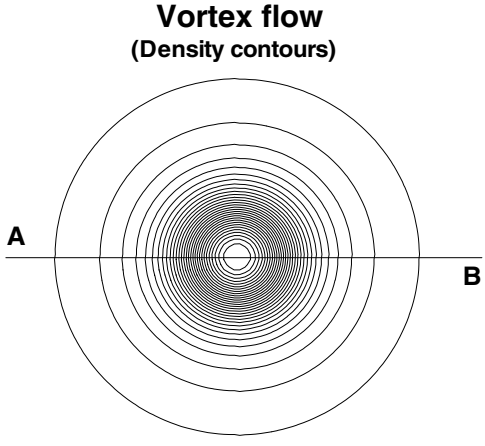

Fig. 21. Density contours of vortex flow.

Since viscous diffusion is not introduced, entropy is constant and a vortex flow should be maintained forever so long as centrifugal force is balanced with pressure gradient toward a vortex core. Thus, in the Euler equations, the ideal solution is the initial distribution itself.

Figs. 22 and 23 show the results using van Leer limiter, MLP3 and MLP5. We can see the difference depending on interpolation schemes. Figs. 24 and 25 show the accuracy improvement of MLP with M-AUSMPW+. It is shown that MLPs combined with M-AUSMPW+ can provide more accurate results than third order interpolation scheme without limiting (see Eq. (30)). Fig. 23 is the comparison of entropy variation according to interpolation schemes. In case of superbee, the vortex flow becomes stronger continuously meaning that entropy decreases without lower bound. As a result, it becomes unstable and after all, computation fails. As expected, MLP5 yields the least increase of entropy and it gives the best result among the interpolation schemes. This test case suggests that interpolation process should be compatible with flow physics.

Generally, interpolation step has been considered irrelevant to flow physics and treated mainly from the mathematical point of view. In actual computations, however, ideal approach is that all of the interpolation, spatial discretization and time integration schemes should follow flow physics faithfully. Among these, spatial discretization scheme is developed to satisfy the entropy condition. For example, AUSMPW+ and M-AUSMPW+ satisfy the entropy condition [22]. Entropy may decrease throughout time integration process, such as the redistribution of residual by an implicit scheme. Lastly, interpolation scheme definitely decreases entropy in some case as explained in Section 3.1.

Figs. 26 and 27 are the results of grid convergence test. Fig. 27(a) shows the L_1 norm of density error when MLP3 is applied to AUSMPW+, Roe's FDS and M-AUSMPW+. As expected, due to slope limiting effect by the multi-dimensional limiting function, MLP3 is slightly less accurate than third order interpolation scheme without limiting. As grid system becomes denser, MLP3 asymptotically approaches

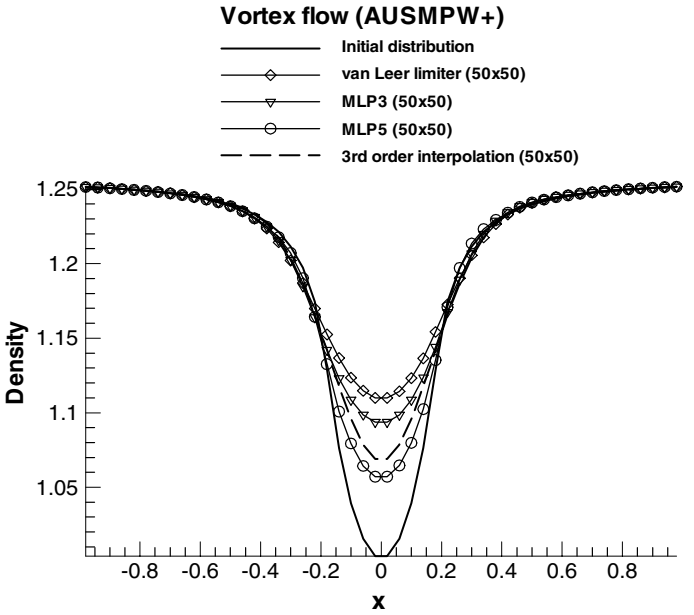

Fig. 22. Comparison of density distributions along the line AB.

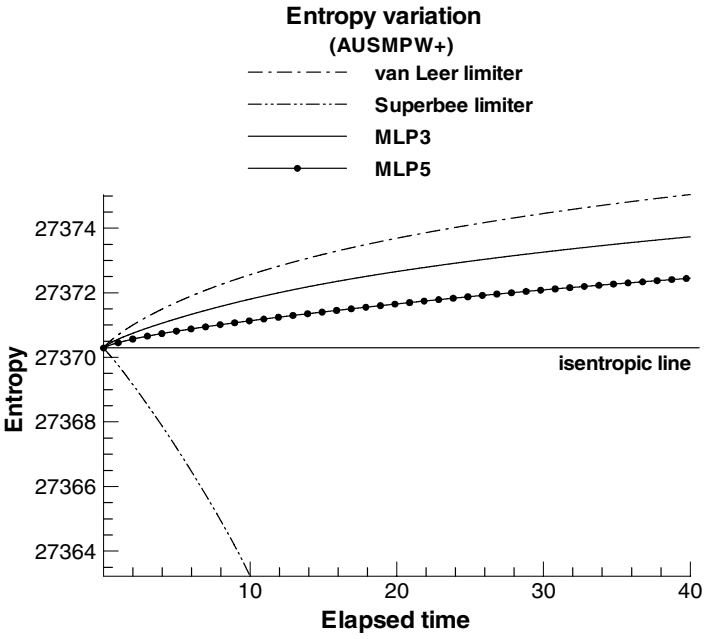

Fig. 23. Comparison of entropy variations of several interpolation schemes.

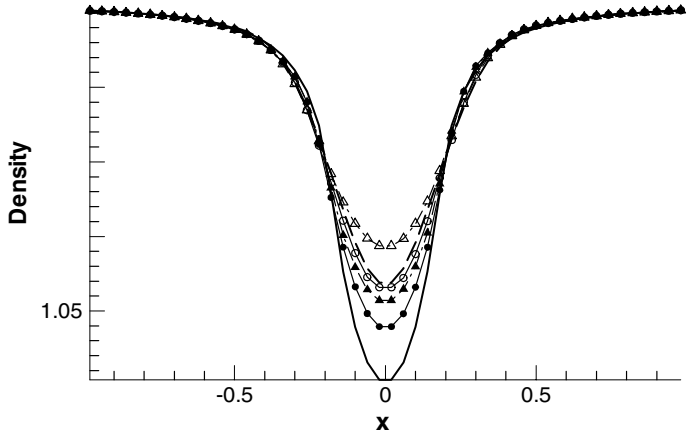

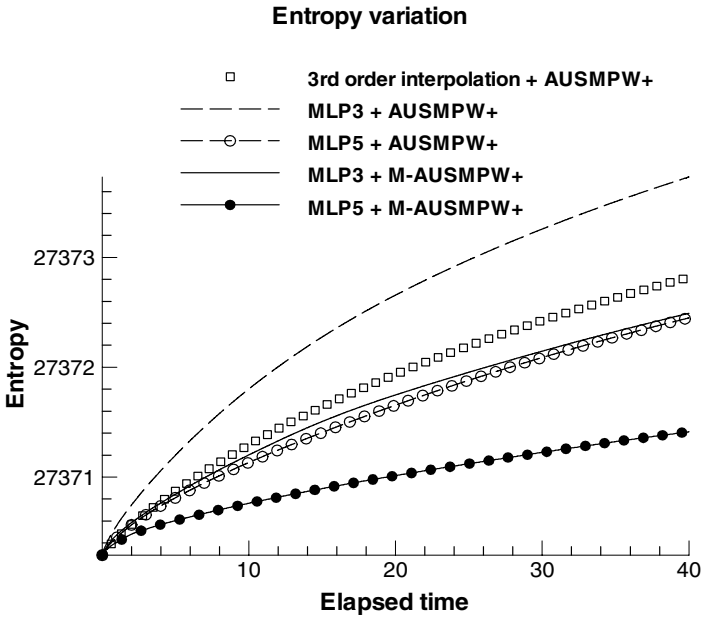

Fig. 25. Comparison of entropy variations (MLPs with AUSMPW+ and M-AUSMPW+).

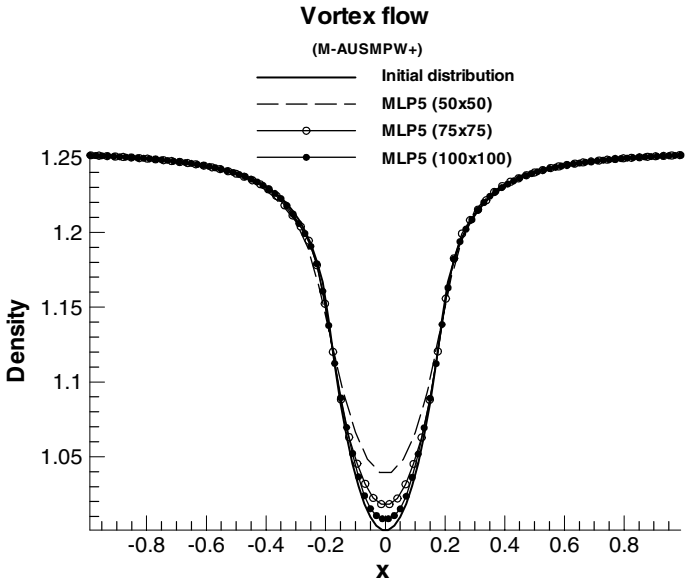

Fig. 26. Comparison of density distributions along the line AB.

that third order interpolation scheme. On the other hand, MLP3 with M-AUSMPW+ shows more accurate result than third order interpolation with AUSMPW+ or Roe's FDS, i.e., previous conventional upwind schemes.

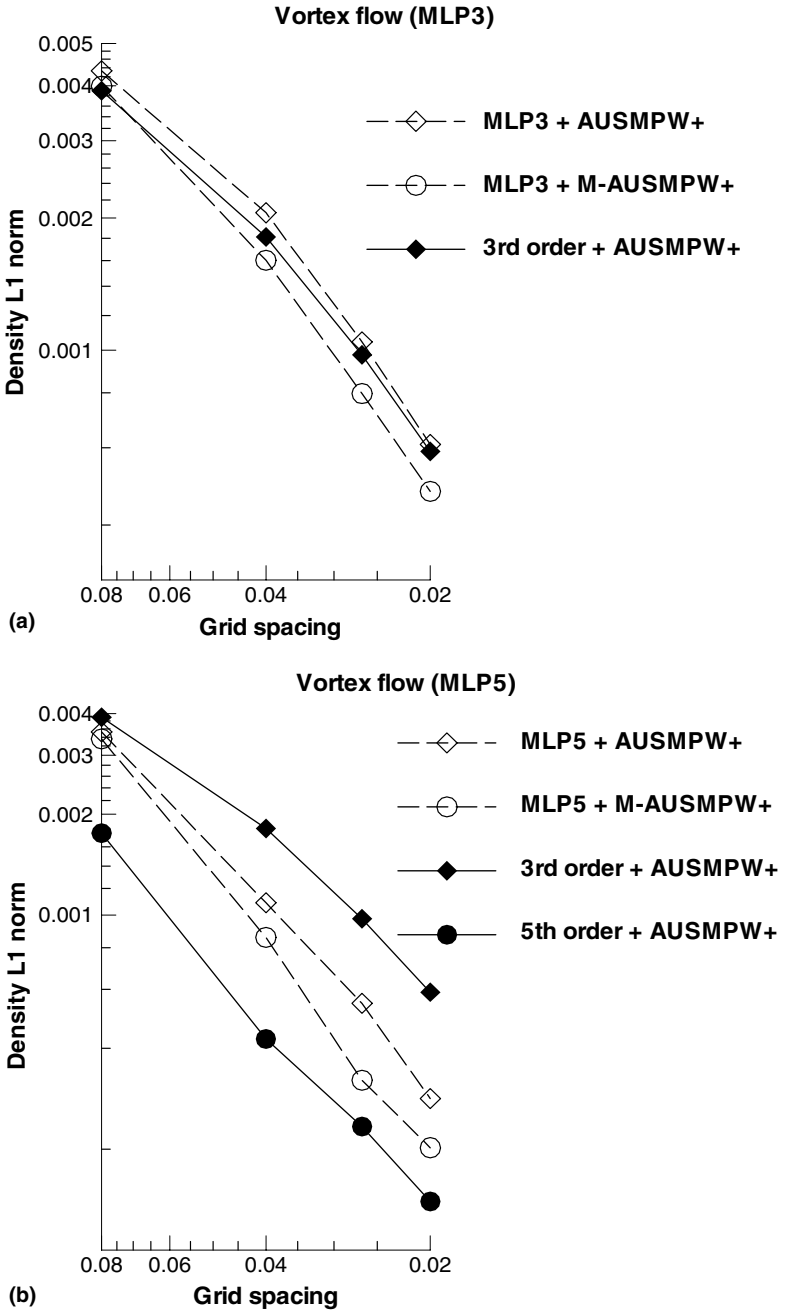

Fig. 27. (a) Grid convergence of MLP3 (AUSMPW+ and M-AUSMPW+). (b) Grid convergence of MLP5 (AUSMPW+ and M-AUSMPW+).

Similarly, Fig. 27(b) show the L_1 norm of density error when MLP5 is applied to AUSMPW+, Roe's FDS and M-AUSMPW+. MLP5 is seen to provide accuracy between third and fifth order spatial accuracy. Especially, MLP5 with M-AUSMPW+ is close to fifth order interpolation with AUSMPW+.

Based on the previous computations, MLP looks very promising in the computation of multi-dimensional flows including both discontinuous and continuous regions.

4.5. Shock-wave/boundary-layer interaction

The free stream Mach number is two and the shock is impinging on the wall with the impinging angle of 32.585. The impinging point is the non-dimensional length of 1 from the leading edge of flat plate. Reynolds number is 2.96×10^5. The adiabatic wall condition is applied for wall boundary condition. The grid system is 56×59 and the denser grid is 150×200.

Figs. 28–30 show the comparison of pressure contours by several interpolation schemes. In Fig. 30, the MLP5 shows a clear flow structure including a reflected shock, an expansion fan, and compression waves through the separation region.

Fig. 31 shows the comparison of pressure distribution along the line AB. The results with minmod and van Leer limiters are diffusive, and superbee is non-monotonic. All of MLPs show monotonic and accurate results. Figs. 32 and 33 show pressure distribution along the line CD. The results with van Leer limiter are so diffused that the expansion and compression of pressure is grossly deviated from the grid converged solution. This is because the separation region is resolved too narrowly. In case of superbee limiter, a flow is compressed and expanded excessively, and the separation region is predicted too much widely. MLP with M-AUSMPW+ matches well with the grid converged solution.

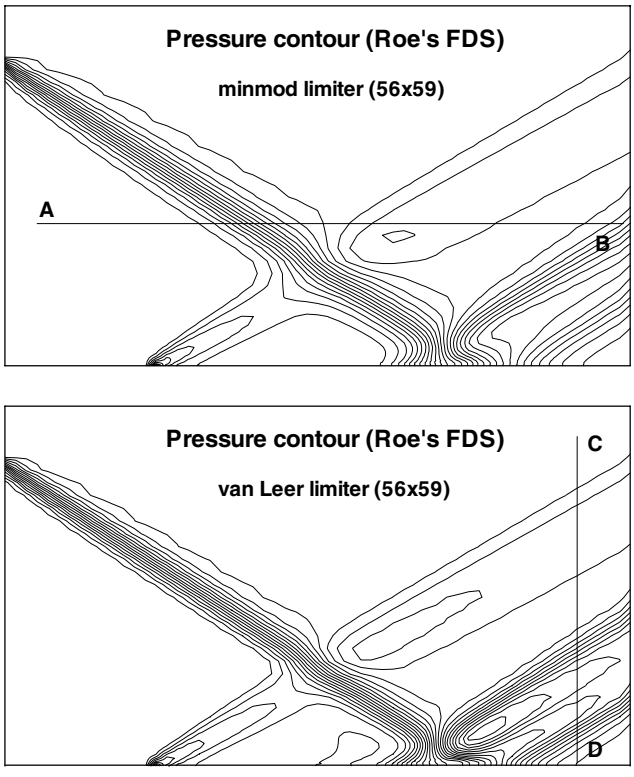

Fig. 28. Pressure contours (minmod and van Leer limiters).

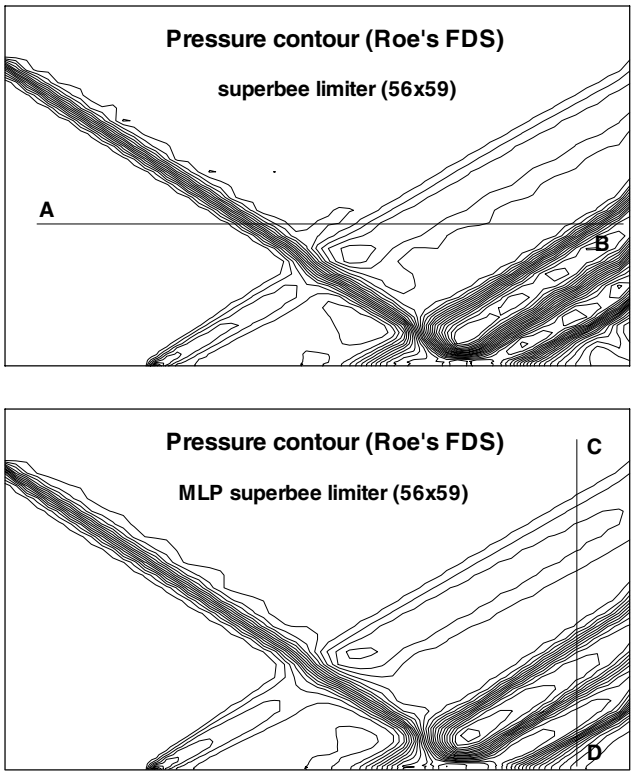

Fig. 29. Pressure contours (superbee and MLP-superbee limiters).

Figs. 34 and 35 show the distribution of skin friction coefficient. Again, the results with van Leer or superbee limiters do not predict the size of separated region properly while MLP3 and MLP5 on the same coarse grid system yield a better agreement with the denser grid result.

Lastly, the error histories of each scheme are compared in Fig. 36. CFL is 3.0 and AF-ADI is used for the time integration. Unlike the case of superbee limiters, the results of MLP3 and MLP5 are converged stably. Since the separated region captured by MLP is wider than van Leer case, it takes a little more iterations.

Overall, MLP shows the similar convergence characteristic to TVD limiter.

4.6. Double Mach reflection

Wall deflection angle is 30° and the initial conditions are as follows.

$$(\ ,u,v,p)_{\mathrm{L}} = (5.149, 4.43182, 0.0, 25.0893), (\ ,u,v,p)_{\mathrm{R}} = (1., 0.0, 0.0, 0.714).$$

The grid system is 300×250 and third order TVD Runge–Kutta time integration is used. Fig. 37 is the comparison of density contours calculated by van Leer limiter and MLP5 at the non-dimensionalized time of 10. MLP5 with M-AUSMPW+ shows more accurate results, especially, in a slip discontinuity region. Fig. 38(a) is pressure distribution along the line AB and Fig. 38(b) shows the detailed comparison of density distribution inside the circle C. Once again, it verifies multi-dimensional monotonic characteristic of MLP. Also, as in Fig. 38(c), MLP captures the second Mach wave and the slip discontinuity more clearly.

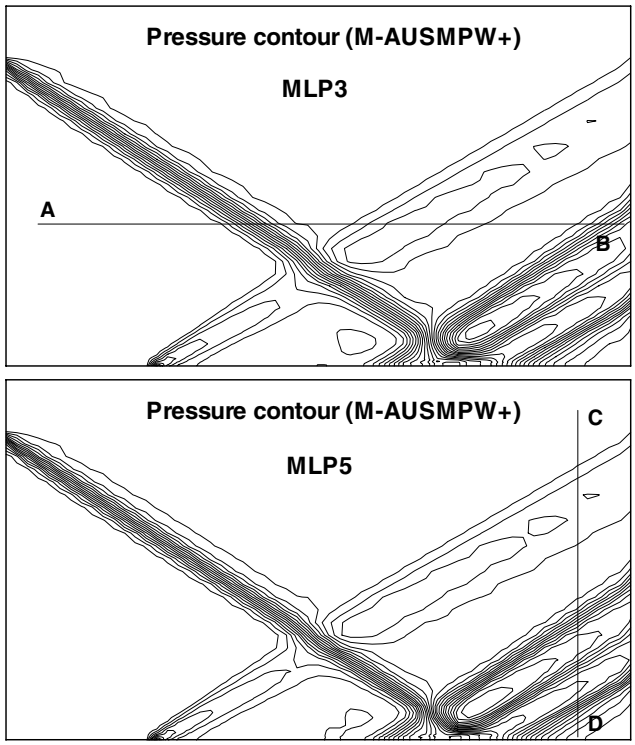

Fig. 30. Pressure contours (MLP3 and MLP5).

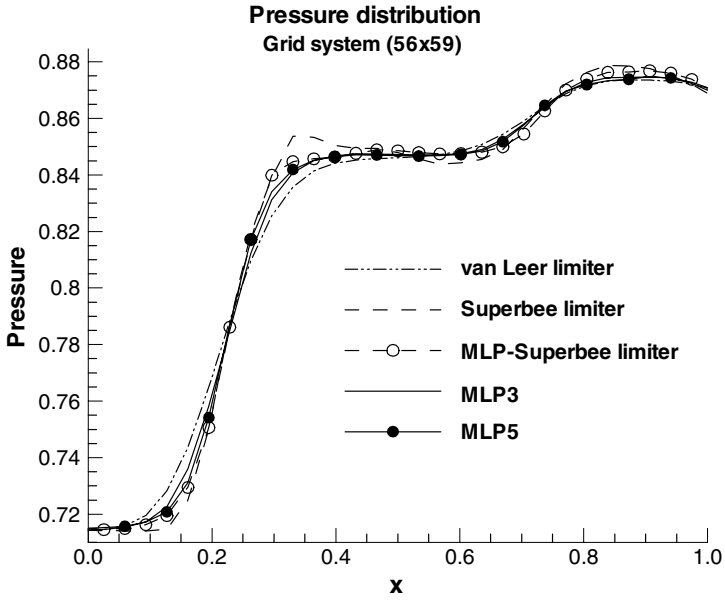

Fig. 31. Pressure distributions along the line AB.

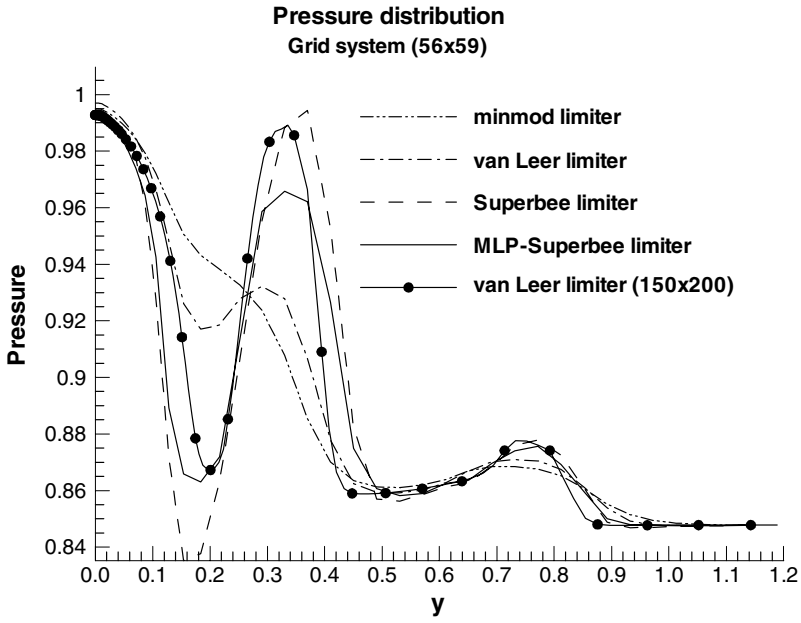

Fig. 32. Pressure distributions along the line CD (TVD limiters).

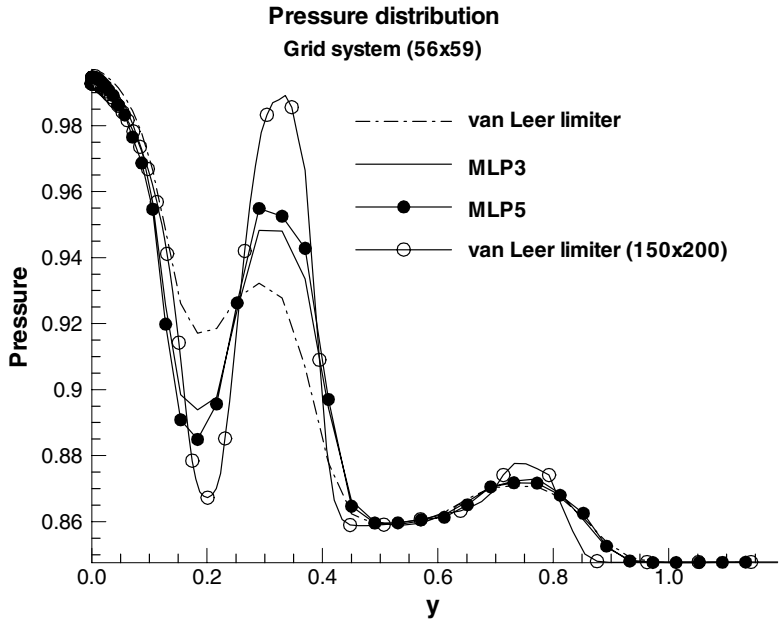

Fig. 33. Pressure distributions along the line CD (MLP3 and MLP5).

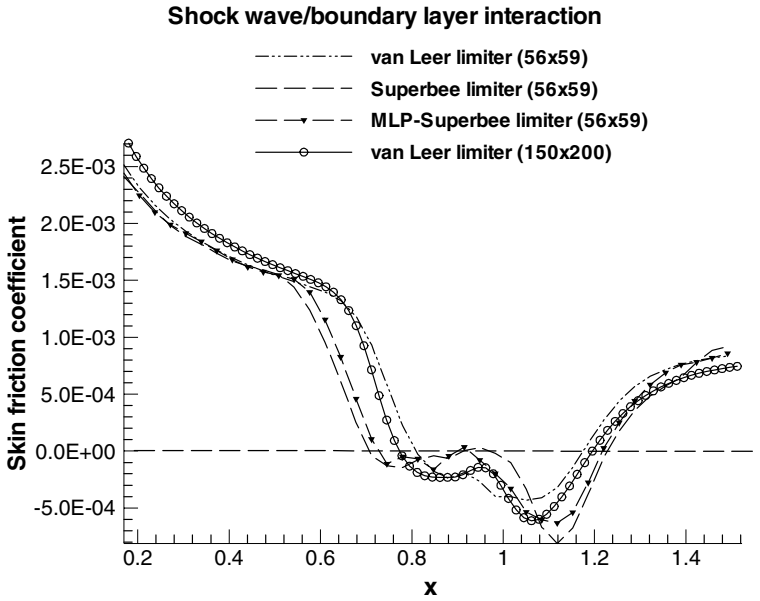

Fig. 34. Comparison of skin friction coefficients (TVD limiters).

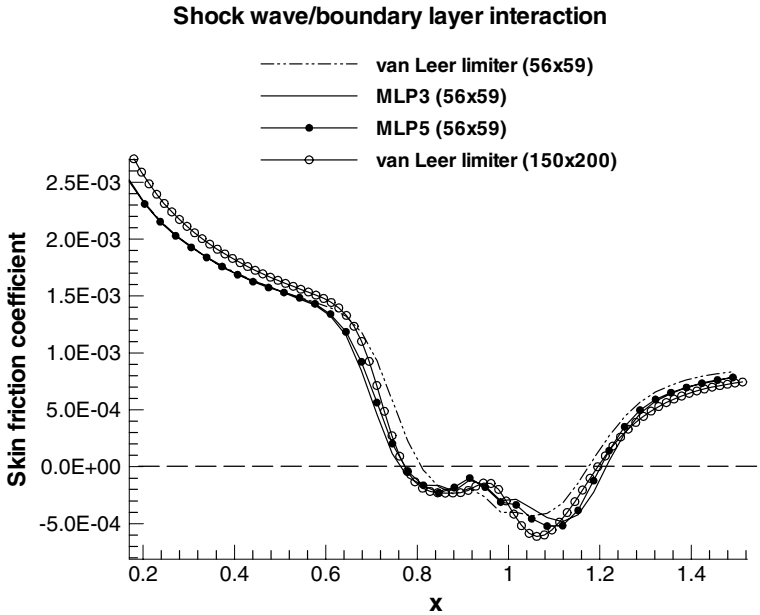

Fig. 35. Comparison of skin friction coefficients (MLP3 and MLP5).

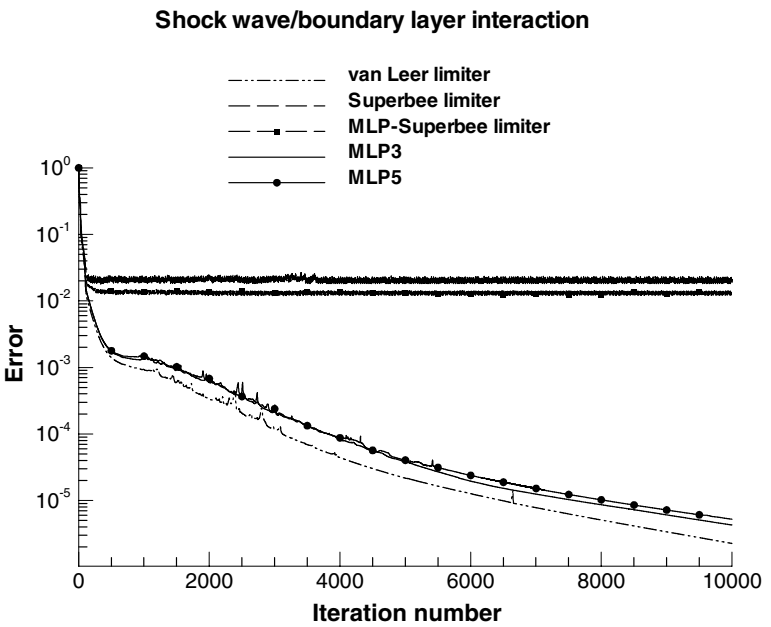

Fig. 36. Error history of several interpolation schemes.

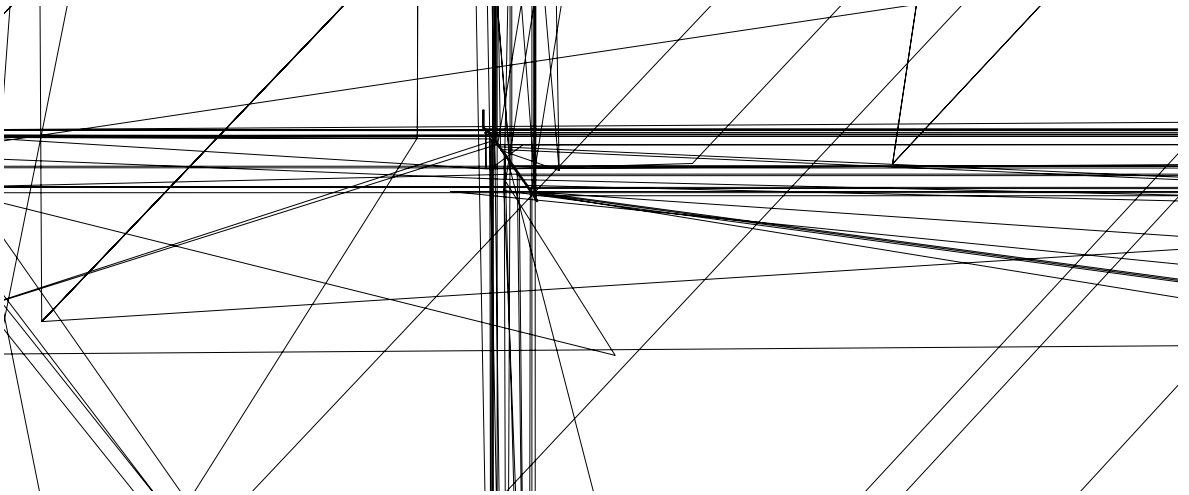

4.7. Normal shock wave/vortex flow interaction

In this test case, a normal shock wave with the Mach number of 1.29 is propagating into a stationary vortex, producing a complex flow pattern induced by shock/vortex interaction. Computational domain is from $(0,0)$ to $(40,40)$. Initially, vortex core is located at the point of $(14,14)$ and the normal shock wave inclined by 45° angle moves toward vortex from the point of $(10,10)$.

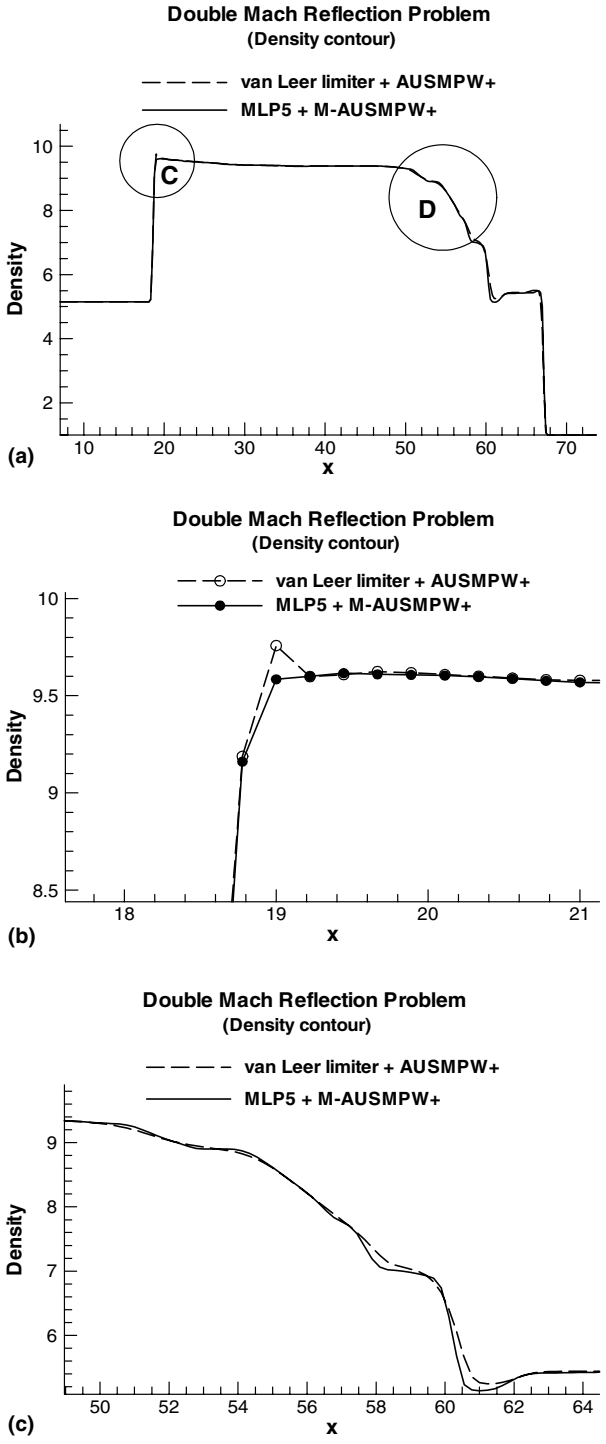

Fig. 38. (a) Density distributions along the line AB. (b) Density distributions in the region of circle C. (c) Density distributions in the region of circle D.

The initial vortex flow is Thomson-Rankine vortex model of Eq. (79) which has the core radius of 0.277 m and the angular velocity of 0.52 rad/s. It is calculated for 15 non-dimensional time, and third order TVD Runge–Kutta time integration is used. In case of MLP, CFL number is 0.5. For van Leer limiter, CFL number is 0.2.

The one of main targets in this problem is to predict pressure in core region as accurately as possible. If we consider the analysis of a blade/vortex interaction or flapping wing aerodynamics, our main concern is definitely focused on the variation of aerodynamic coefficients induced by vortex flow. When vortex hits a blade or a wing, aerodynamic coefficients change significantly because of low pressure in core region. Another example is vortex flow on flapping wing. Vortex stays on the upper surface of wing and produces a very high lift. Thus, the accurate computation of the core pressure is crucial in understanding the complex nature of the high-lift flapping aerodynamics.

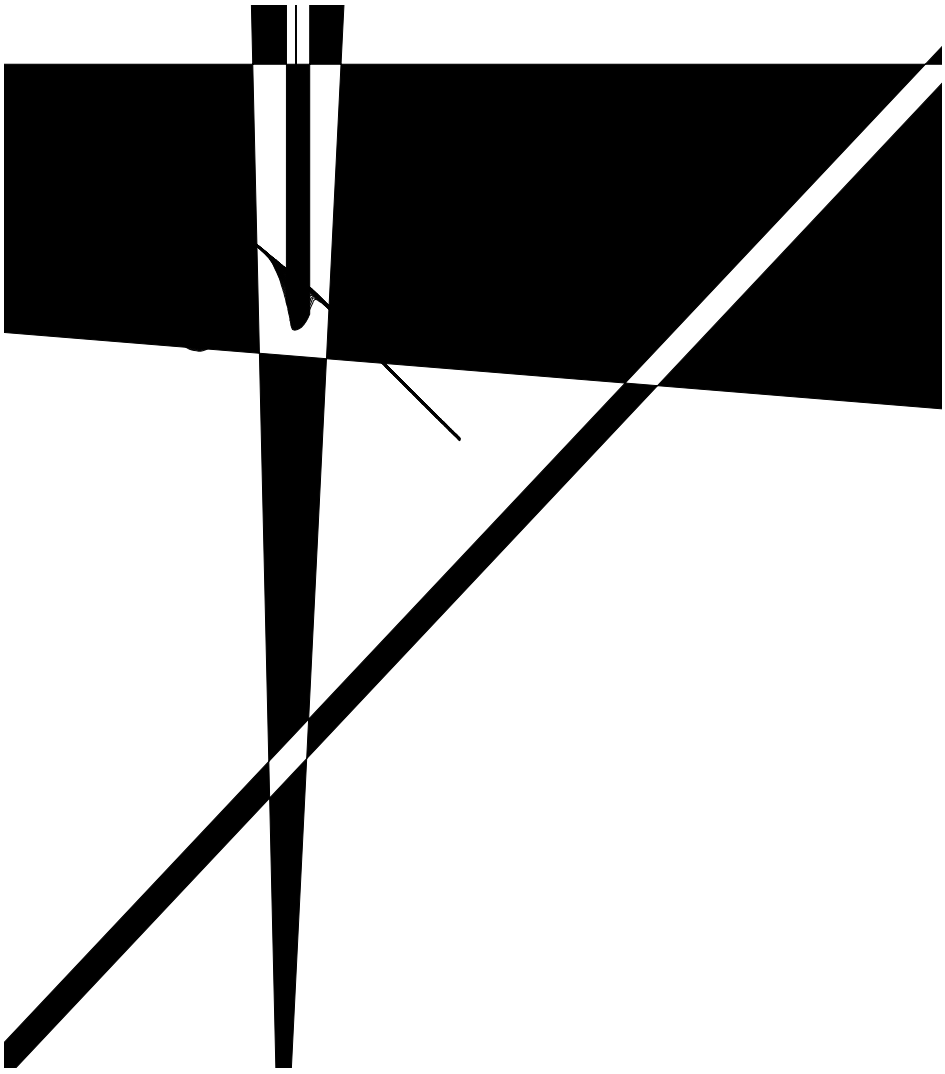

Fig. 39(a) and (b) are results on the coarse (200×200) and fine (400×400) mesh. The left figure is obtained by van Leer limiter with AUSMPW+ and the right one is by MLP5 with M-AUSMPW+. The high performance of MLP is certified again in Fig. 39. Even with a smaller CFL number, van Leer limiter cannot prevent oscillatory phenomena. Even for the flow with vortex and shock discontinuity, computation is performed stably since MLP can control oscillations across a discontinuity and maintain higher accuracy in continuous region. Flow structure can be seen very clearly with MLP. Fig. 40 shows the more quantitative comparison of density distribution in core region. The core pressure calculated by AUSMPW+ is somewhat smeared but MLP5 with M-AUSMPW+ gives about four times more accurate result compared with van Leer limiter case.

4.8. Viscous shock tube problem

The viscous shock tube problem [23,24] tested in Part I is revisited to examine the accuracy of MLP in complex shock viscous flows. The Reynolds number is 200 with constant viscosity and the initial state is given as follows.

$$(\ \ ,u,v,p)_{\mathrm{L}} = (120,0,0,120/\gamma) \text{ and } (\ \ ,u,v,p)_{\mathrm{R}} = (1.2,0,0,1.2/\gamma).$$

Viscous fluxes are calculated by 4th order spatial accuracy, and third order TVD Runge–Kutta method is used.

Fig. 41 is the comparison of density contours. Case (a)–(c) are results by van Leer limiter with AUSMPW+ on coarse (250×125), medium (350×175) and fine (500×250) grid system, and case (d)–(f) are results by MLP5 with M-AUSMPW+ on the same grid systems. MLP5 with M-AUSMPW+ on coarse grid system shows a much better result than van Leer limiter with AUSMPW+ on medium grid system, which

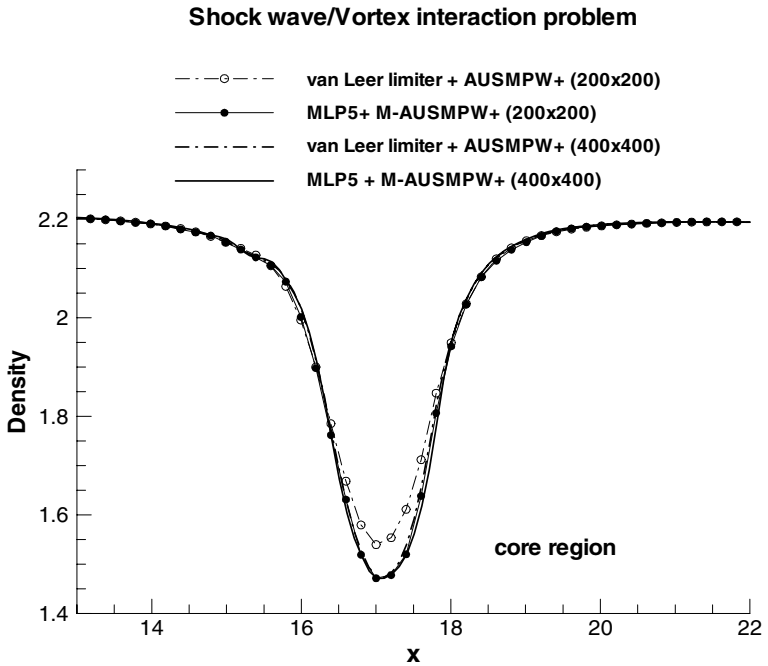

Fig. 40. Comparison of density distributions in core region (van leer limiter with AUSMPW+ and MLP5 with M-AUSMPW+).

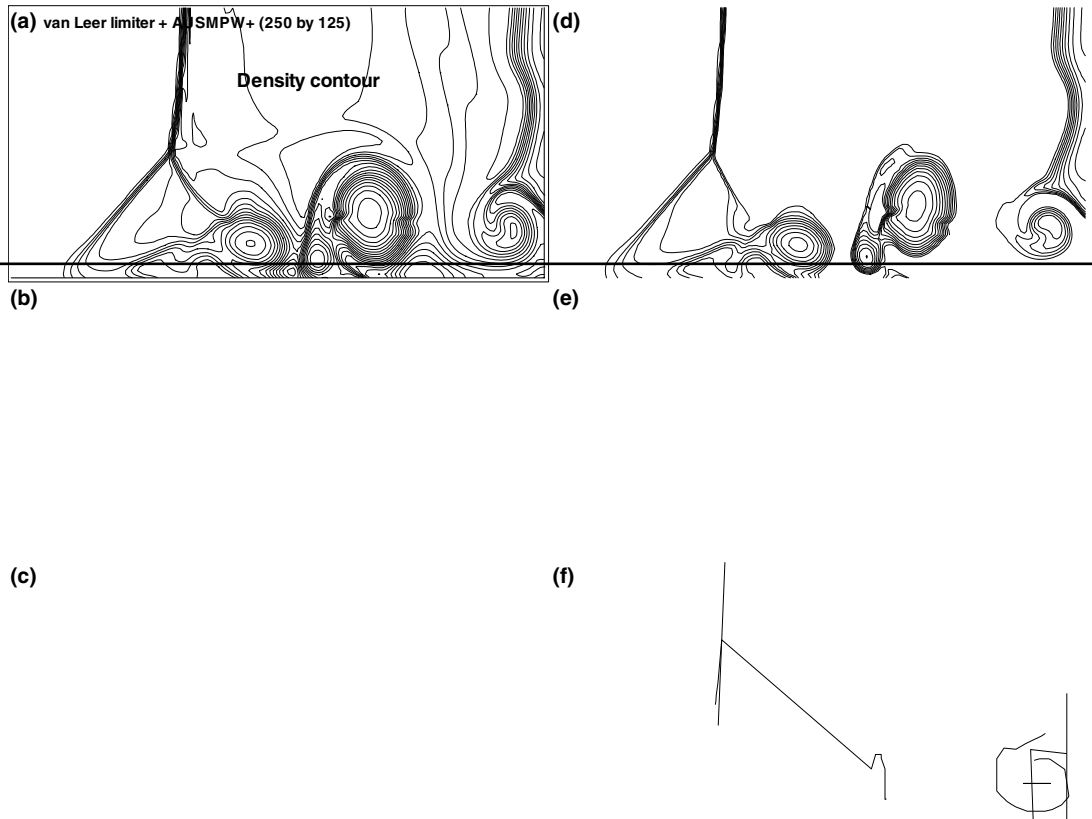

has twice more grid points. Furthermore, it is very similar to the fine grid result which has four times more grid points. MLP on medium grid system also shows a better result than van Leer limiter with AUSMPW+ on fine grid system, and almost reaches the grid converged result (MLP on fine grid system).

Judging from the direct comparison, MLP5 with M-AUSMPW+ can give about three times grid point reduction effect. If the influence of iteration number is included, actual grid reduction effect increases even further. When the same scheme is used, iteration number is generally proportional to grid size in unsteady flow calculations. For that reason, the total iteration number for case (c) and case (f) are almost double compared to case (a) and case (d). Thus, it may say that MLP5 with M-AUSMPW+ saves the total computational cost about six times in providing the same level of accuracy. Comparison with other interpolation schemes such as WENO or ACM can be referred to [24].

In Fig. 42, density distributions along the wall are compared with one another. The improvement observed from Fig. 41 is certified again. The result by MLP5 with M-AUSMPW+ on coarse grid system is more accurate than the result by van Leer limiter with AUSMPW+ on medium grid system.

Table 2 is the comparison of the primary vortex size. The height and angle of the primary vortex, which is sensitive to numerical dissipation, is converged to 0.168. Even on fine grid system, van Leer limiter with AUSMPW+ yields smaller vortex while MLP5 with M-AUSMPW+ on medium grid system gives the identical results in terms of vortex height and angle. Comparing vortex size, case (d) to case (f) provide about four times grid point reduction effect over case (a) to case (c).

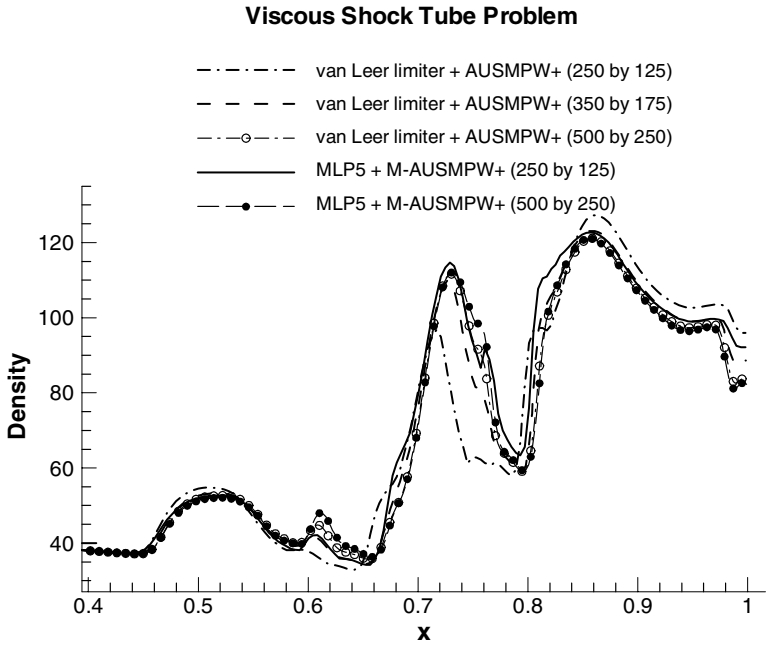

Fig. 42. Comparison of density distributions along a wall.

Table 2
Comparison of the height of the primary vortex

Scheme	Case (a) (250×125)	Case (b) (350×175)	Case (c) (500×250)	Case (d) (250×125)	Case (e) (350×175)	Case (f) (500×250)
Height (h)	0.142	0.155	0.163	0.161	0.168	0.168

5. Conclusions

By analyzing conventional TVD limiters and exploiting higher order TVD interpolation based on the information on local curvature distribution, a new multi-dimensional limiting function is derived. And, a new multi-dimensional limiting process (MLP) is developed by combining the multi-dimensional limiting function with a higher order polynomial interpolation. The newly developed method turns out to have several desirable characteristics such as multi-dimensional monotonicity across a discontinuity, robust convergence and computational efficiency comparable to conventional TVD limiters. In addition, higher order interpolation can be easily incorporated.

The most distinguishable property of MLP is to provide non-oscillatory profiles in multi-dimensional flows and, as a result, a good convergence characteristic. Thanks to the properties, MLP combined with M-AUSMPW+ can significantly increase accuracy, convergence/robustness and efficiency both in steady and unsteady multi-dimensional flows containing physical discontinuities. Through numerous test cases including a vortex flow, a shock-wave/boundary-layer interaction, shock wave/vortex interaction and viscous shock tube problem, it is verified that MLP can control numerical oscillations in multi-space dimensions. In addition to robustness improvement across a discontinuity, accuracy enhancement in pure multi-dimensional problems such as separated flows or vortex flows is remarkable, especially combined with

M-AUSMPW+. From the numerous computed results, MLP with M-AUSMPW+ generally provides three or four times accuracy improvement in terms of grid points, compared with TVD with popular flux functions. Also, it does not show the entropy decreasing phenomenon in an expansion flow region.

Through the extension of current outcomes to three-dimensional flows, MLP is expected to bring substantial reduction of computational cost and accuracy improvement simultaneously.

Acknowledgements

The authors appropriate the financial support by Agency for Defense Development (ADD) and by the Brain Korea-21 Program for the Mechanical and Aerospace Engineering at Seoul National University. We give the special thank to Dr. Sungsoo Kim for the help of revising the present paper. We also appreciate referees for their critical comments and valuable suggestions.

References

[1] P.L. Roe, Discrete models for the numerical analysis of time-dependent multidimensional gas dynamics, Journal of Computational Physics 63 (1986) 458–476.
[2] C. Rumsey, Development of a Grid-Independent Approximate Riemann Solver, Ph.D. Thesis, University of Michigan, 1991.
[3] C. Lacor, Ch. Hirsch, Genuinely upwind algorithms for multidimensional Euler equations, AIAA Journal 30 (1) (1991) 56–63.
[4] Dadone, B. Grossman, Characteristic-based, rotated upwind scheme for the Euler equation, AIAA Journal 30 (9) (1992).
[5] D.W. Levy, K.G. Powell, B. Van Leer, Use of a rotated Riemann solver for the two-dimensional Euler equations, J. of Computational Physics 106 (1993) 201–214.
[6] D. Sidilkover, A genuinely multidimensional upwind schemes and efficient multigrid solver for the compressible Euler equations, Journal of Computational Physics (submitted).
[7] H. Deconinck, H. Paillere, R. Struijs, P.L. Roe, Multidimensional upwind schemes based on fluctuation-splitting for systems of conservation laws, Computational Mechanics 13 (1993) 323–340.
[8] Y. Tamura, K. Fuji, A multi-dimensional upwind scheme for the euler equations on structured grids, Computers and Fluids 22 (2/3) (1993) 125–137.
[9] A. Harten, High resolution schemes for hyperbolic conservation laws, Journal of Computational Physics 49 (3) (1983) 357–393.
[10] P.K. Sweby, High resolution schemes using flux limiters for hyperbolic conservation laws, SIAM Journal on Numerical Analysis 21 (5) (1984) 995–1011.
[11] A. Harten, B. Enquist, S. Osher, S.R. Chakravarthy, Uniformly high order accurate essentially non-oscillatory schemes, III, Journal of Computational Physics 71 (2) (1987) 231–303.
[12] C.W. Shu, TVB uniformly high order schemes for conservation laws, Mathematics of Computation 49 (179) (1987) 105–121.
[13] A. Harten, S. Osher, Uniformly high order accurate non-oscillatory schemes I, SIAM Journal on Numerical Analysis 24 (1987) 279–309.
[14] C.W. Shu, S. Osher, Efficient implementation of essentially non-oscillatory shock-capturing schemes, Journal of Computational Physics 77 (1988) 439–471.
[15] X-D. Liu, S. Osher, T. Chan, Weighted essentially non-oscillatory schemes, Journal of Computational Physics 115 (1994) 200–212.
[16] G.S. Jiang, C.W. Shu, Efficient implementation of weighted ENO schemes, Journal of Computational Physics 126 (1996) 202–228.
[17] K.H. Kim, C. Kim, Development of the numerical scheme for multi-dimensional flows. Part I: Spatial discretization scheme, Journal of Computational Physics 208 (2005) 527–569.
[18] B. van Leer, Toward the ultimate conservative difference scheme, Journal of Computational Physics 32 (1979) 101–136.
[19] A. Jameson, Analysis and design of numerical schemes for gas dynamics 1 artificial diffusion, upwind biasing, limiters and their effect on accuracy and multigrid convergence, International Journal of Computational Fluid Dynamics 4 (1995) 171–218.
[20] J.B. Goodman, R.J. LeVeque, On the accuracy of stable schemes for 2D scalar conservation laws, Mathematics of Computation 45 (1985) 15–21.
[21] S.P. Spekreijse, Multigrid solution of monotone second order discretizations of hypersonic conservations laws, Mathematics of Computation 49 (1987) 135–155.
[22] K.H. Kim, C. Kim, O.H. Rho, Methods for the accurate computations of hypersonic flows, Part I: AUSMPW+ Scheme, Journal of Computational Physics 174 (2001) 38–80.

[23] V. Daru, C. Tenaud, Evaluation of TVD high resolution schemes for unsteady viscous shocked flows, Computers and Fluids 30 (2001) 89–113.
[24] B. Sjögreen, H.C. Yee, Grid convergence of high order methods for multiscale complex unsteady viscous compressible flows, Journal of Computational Physics 185 (2003) 1–26.